Coupled Relative Orbit and Attitude Control Augmented by the Geomagnetic Lorentz Propulsions

Xu Huang[*] and Zheng You[†]
Tsinghua University, 100084 Beijing, People's Republic of China
Liangliang Chen[‡]
China Academy of Space Technology, 100094 Beijing, People's Republic of China
and
Jinlong Yu[§]
Space Engineering University, 101416 Beijing, People's Republic of China

An electrostatically charged spacecraft is subject to the Lorentz force and torque when moving in the geomagnetic field. By active modulation of the surface charge, the induced Lorentz force and torque can be used for orbit and attitude control, respectively. Because of the electromagnetic mechanism, the orbit and attitude motion of such spacecraft are naturally coupled, and the induced Lorentz force and torque are both instantaneously underactuated. Thus, other kinds of actuation are required to render the system fully actuated and controllable. A hybrid control system is then proposed in this paper for Lorentz-augmented spacecraft relative orbit and attitude control. The relative orbit motion is controlled by the combination of the Lorentz force and the thruster-generated control force, and the relative attitude motion is governed by the combination of the Lorentz torque and the magnetic torque. By using the adaptive backstepping control method, a closed-loop control scheme is designed for the hybrid control system to deal with the dynamic coupling, underactuation, unknown external disturbances, and model approximation errors simultaneously. The parameter adaptation laws are derived via the Lyapunov theory to guarantee the stability of the closed-loop system. Optimal distribution laws of the hybrid control inputs are then analytically solved. Finally, numerical examples are simulated in a J_2-perturbed environment to verify the feasibility of the proposed hybrid control system and the validity of the closed-loop control scheme.

I. Introduction

THE environmental forces and torques, such as atmospheric drag, geomagnetic Lorentz force, and magnetic torque, can be used for spacecraft orbit and attitude control [1–3]. Using environmental forces and torques as auxiliary propulsions helps in saving the propellant on board, enhancing the maneuvering ability, and improving the system lifetime [4–6]. Because of these favorable advantages, a series of potential applications has been proposed [7]. For example, the atmospheric drag or the geomagnetic Lorentz force can be used for spacecraft rendezvous [8–10], hovering [11], and formation control [12]. Also, the magnetic torque is capable of spacecraft detumbling and momentum desaturation [13]. Recently, another novel means of electromagnetic actuation, the Lorentz torque, is proposed for attitude control [14]. Three pairs of spherical Coulomb shells are installed along the three principal axes of the spacecraft [15]. The Coulomb shells are actively charged to generate the Lorentz force via interaction with the geomagnetic field. Because the center of mass (c.m.) of each Coulomb shell is not coincided with the c.m. of the spacecraft, the induced Lorentz force acting on each shell will also generate the Lorentz torque at the c.m. of the spacecraft [16]. The induced Lorentz torque can then be used for attitude control. As can be seen, once the Coulomb shells are charged, both the Lorentz forces and torques will be induced simultaneously. Thus, the orbit and attitude motion of such spacecraft, referred to as the Lorentz spacecraft, are naturally coupled.

As well known, the magnitude of the Lorentz force is determined by the local magnetic-field intensity and the vehicle's velocity relative to the local magnetic field. Generally, stronger magnetic field and faster relative velocity indicate larger Lorentz force. On the one hand, the Earth's magnetic field in low Earth orbit (LEO) is much stronger than that in higher orbits. Here, the orbital altitude of the LEO ranges from 100 to 2000 km. On the other hand, the spacecraft in LEO travels much faster than that in higher orbits. Thus, such Lorentz spacecraft is more efficient in LEO than in higher orbits.

As compared with other environmental propellantless propulsions, the Lorentz force and torque are also more favorable in LEO. For example, the atmospheric drag, dominated by the local atmospheric density and the vehicle's velocity with respect to the local atmosphere, is more dominant and effective in super low orbits below 100 km where the atmosphere is much denser. The solar pressure, generally on the order of 10^{-8} m/s^2 in LEO, is too tiny to take significant effect in LEO [12]. Furthermore, the interspacecraft Coulomb force can hardly be used in LEO due to the significant Debye shielding effect in LEO where the Debye length is about several centimeters [12]. Therefore, in consideration of the space environment in LEO, the Lorentz spacecraft is more advantageous.

Nevertheless, a series of technical challenges needs to be surmounted before the realization of such Lorentz spacecraft, including the charge generation device, the charge storage mechanism, and the onboard power system. Also, the spacecraft structure design with the six Coulomb shells is another challenging issue. A large separate distance between the Coulomb shells will undermine the rigidity of the spacecraft structure and increase the control effort for spacecraft stabilization. In contrast, a small separate distance will cause electromagnetic compatibility problems. Hence, in spite of the compelling advantages over other environmental propulsions, the drawbacks on the structure design and physical realization of such Lorentz spacecraft are also inevitable. It is generally accepted that a charging level on the order of 10^{-3} to 10^{-2} C/kg is near-term feasible by concentrated research [17], and the maximum specific charge is about 0.03 C/kg [7]. This charging level can afford spacecraft relative motion control within several kilometers [12]. Thus, the size of the relative orbit discussed in this paper is restricted to several kilometers.

*Postdoctor, Department of Precision Instrument; xunudt@126.com.
†Professor, Department of Precision Instrument; yz_dpi@163.com.
‡Senior Engineer, Department of Information Engineering; cll_cast@163.com.
§Ph.D. Candidate, College of Aerospace Engineering; yunudt@126.com.

Besides the aforementioned drawbacks, another inevitable constraint imposed on the application of Lorentz spacecraft is the inherent underactuation problem [18,19]. Because of the physical mechanism, the induced Lorentz force is instantaneously perpendicular to the local magnetic field and the spacecraft's velocity relative to the local magnetic field. Also, the induced Lorentz torque is instantaneously constrained in a plane containing the local magnetic field. Thus, both the Lorentz force and torque are instantaneously underactuated. Obviously, this inherent underactuation problem further complicates the controller design.

To deal with the underactuation, the most direct solution is supplementing other kinds of auxiliary propulsion. For the orbit control of Lorentz spacecraft, a usual supplement is the thruster-generated control force. For example, by using the hybrid control inputs consisting of the Lorentz force and impulsive thrust, Sobiesiak and Damaren [20,21] investigated the Lorentz-augmented spacecraft formation control problem, and optimal distribution laws of these two kinds of propulsion are derived via the linear quadratic regulator control method. Differently, in combination with continuous thrust, Huang et al. [11,22] designed optimal controllers for Lorentz-augmented spacecraft formation or hovering. Also, optimal distribution laws of the hybrid control inputs are derived analytically via the Pontryagin maximum principle. For the attitude control of Lorentz spacecraft, the magnetic torque generated by the three orthogonal current-driven coils on board is introduced to render the attitude control system fully actuated. Notably, the induced magnetic torque is also instantaneously underactuated because the direction of magnetic torque is perpendicular to that of the local magnetic field. As can be seen, the Lorentz torque acts in a plane containing the magnetic field, whereas the magnetic torque acts in a plane orthogonal to the magnetic field. Therefore, the Lorentz torque and the magnetic torque lie in two mutually perpendicular planes. That is to say, the Lorentz torque and the magnetic torque can compose a control torque in an arbitrary direction. In this way, the underactuation problem is solved by combination of these two kinds of electromagnetic torques. Huang and Yan [19] proposed the concept of this hybrid attitude control system, and solved the optimal distribution laws of the Lorentz and magnetic torque via geometry method.

As can be seen, despite that the underactuation problem has been solely solved for either the orbit or attitude control of Lorentz spacecraft, the coupled orbit and attitude control remains an open question. After all, the orbit and attitude motion are naturally coupled. The orbit control may affect the attitude motion, and vice versa. Therefore, it is necessary to design control schemes to deal with the coupled orbit and attitude motion simultaneously. As aforementioned, the acting direction of the Lorentz force or torque is determined by its electromagnetic generation mechanism, and is resultingly unchangeable. Thus, only the charge of each Columbo shell is adjustable to vary the magnitude of the Lorentz force or torque. Furthermore, it is notable that the modulation of charge will simultaneously change the magnitude of the Lorentz force and the Lorentz torque. Therefore, to fulfill the coupled orbit and attitude control, the charge of each Coulomb shell should meet both the orbit and attitude control requirements simultaneously. This fact poses more difficulties for controller design.

To solve the dynamic coupling and underactuation problem simultaneously, this paper proposes an adaptive backstepping controller (ABC) for the relative orbit and attitude control of Lorentz spacecraft. The control system is driven by hybrid control inputs consisting of the Lorentz force, the thruster-generated continuous control force, the Lorentz torque, and the magnetic torque. The former two kinds of actuation are used for orbit control, and the remaining two are used for attitude control. Given that the Lorentz force and torque can only be modulated by the variance of the charge of each Coulomb shell, the actual control inputs are thus composed of the shells' charges, continuous thrusts, and magnetic dipole moments of the coils. Then, this paper seeks to solve the optimal distribution laws of these control inputs. Thus, in comparison with previous works on Lorentz spacecraft, the main differences and enhancements of this paper can be summarized as follows:

1) Different from previous works solely focused on the orbit or attitude control of Lorentz spacecraft [9,11,14–16,18–22], this paper deals with the orbit and attitude control simultaneously.

2) A hybrid control system consisting of the charge of each Coulomb shell, the thruster-generated control forces, and the magnetic dipole moments is proposed for spacecraft orbit and attitude control, and the optimal distribution laws of these control inputs are solved analytically.

The remainder of this paper is organized as follows. Firstly, the six-degree-of-freedom (six-DOF) dynamic model of Lorentz-augmented relative orbit and attitude motion is developed in Sec. II. Then, to deal with the dynamic coupling, underactuation, external perturbations, and model approximation errors simultaneously, a closed-loop control scheme is designed in Sec. III. Also, the optimal distribution laws of the hybrid control inputs and the corresponding closed-loop system stability analysis are given in this section. Finally, a typical Lorentz-augmented spacecraft hovering mission is simulated in Sec. IV to testify the theoretical analyses and the controller performances, followed by the conclusions that end the paper in Sec. V.

II. Dynamic Model

A. Equations of Relative Motion

As depicted in Fig. 1, the chief is assumed to be an uncharged spacecraft, and the deputy flying nearby is a charged Lorentz spacecraft. $O_E X_I Y_I Z_I$ is an Earth-centered inertial (ECI) frame, and O_E is the center of Earth. O_C and O_D are, respectively, the c.m. of the chief and deputy spacecraft. $O_C xyz$ is a local-vertical-local-horizontal (LVLH) frame, where x axis is along the chief's radial direction, z axis is normal to the chief's orbital plane, and y axis completes the right-handed Cartesian frame. $O_D x_b y_b z_b$ is the deputy's body-fixed (BF) frame, of which the axes are aligned with the principal axes of inertia. Six Coulomb shells are fixed at the ends of three mutually perpendicular rigid rods, respectively. O_i is the c.m. of the ith Coulomb shell. Also, three mutually orthogonal magnetic coils are installed on the three rods. The Coulomb shells are used to generate the Lorentz forces and torques, and the magnetic coils are used for the generation of magnetic torques.
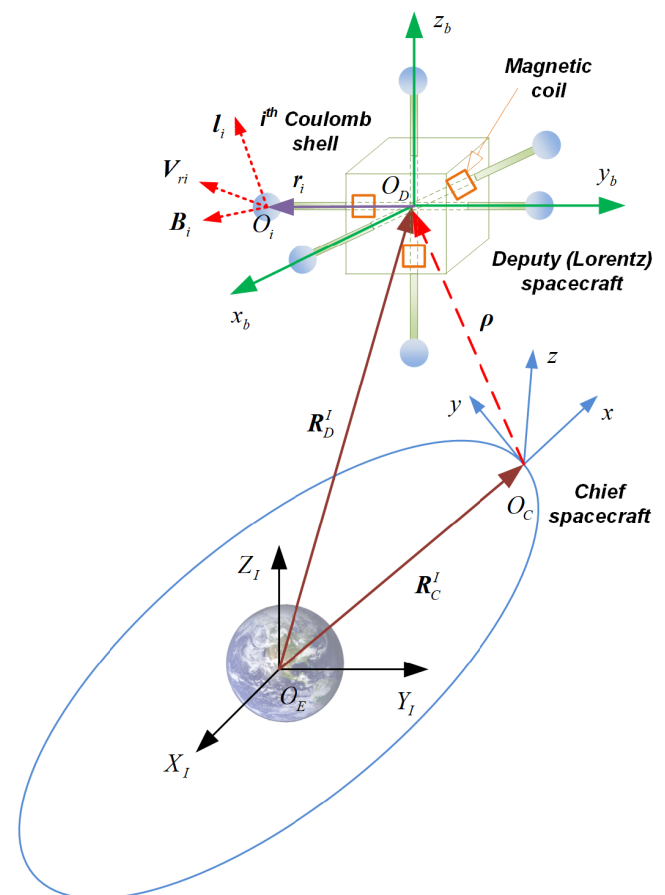

Fig. 1 Definitions of the coordinate frames.

For an arbitrary vector $\boldsymbol{a}$ throughout this paper, the notation $\boldsymbol{a}^X$ denotes the expression of $\boldsymbol{a}$ in the X frame. Also, $\dot{\boldsymbol{a}}|_Y$ refers to the time derivative of $\boldsymbol{a}$ in the Y frame, that is, the rate of change of $\boldsymbol{a}$ as seen by an observer rigidly fixed to the Y frame. Thus, $(\dot{\boldsymbol{a}}|_Y)^X$ denotes the time derivative of $\boldsymbol{a}$ in the Y frame expressed in the X frame. Notably, if no special superscript is used to indicate the corresponding frame, then the vector $\boldsymbol{a}$ is expressed in the deputy's BF frame (i.e., $\boldsymbol{a} = \boldsymbol{a}^B$). Similarly, if no special subscript is used to indicate the corresponding frame, then the vector $\dot{\boldsymbol{a}}$ denotes the time derivative of $\boldsymbol{a}$ in the BF frame (i.e., $\dot{\boldsymbol{a}} = \dot{\boldsymbol{a}}|_B$). According to the above definitions, it holds that $\dot{\boldsymbol{a}} = (\dot{\boldsymbol{a}}|_B)^B$.

$\boldsymbol{R}_C^I$ and $\boldsymbol{R}_D^I$ refer to the orbital radius vector of the chief and deputy, respectively. The superscript I denotes that the vectors $\boldsymbol{R}_C^I$ and $\boldsymbol{R}_D^I$ are expressed in the ECI frame. By using coordination transformation $\boldsymbol{R}_D = \boldsymbol{M}_{BI}\boldsymbol{R}_D^I$, the expression of the deputy's orbit radius vector in the BF frame can be derived as $\boldsymbol{R}_D$, where $\boldsymbol{M}_{BI}$ is the coordination transformation matrix from the ECI frame to the BF frame. Then, $\boldsymbol{R}_i = \boldsymbol{R}_D + \boldsymbol{r}_i$ is the orbital radius vector of the ith Coulomb shell in the BF frame, with $\boldsymbol{r}_i$ being the position vector of the ith Coulomb shell in the BF frame too.

Define $\boldsymbol{\omega}_C$ and $\boldsymbol{\omega}_D$ as the angular velocity of the chief and deputy, respectively. Then, the relative angular velocity between the chief and deputy can be defined as

$$\boldsymbol{\omega} = \boldsymbol{\omega}_D - \boldsymbol{A}(\boldsymbol{q})\boldsymbol{\omega}_C^C \qquad (1)$$

where $\boldsymbol{q} = [\,\bar{\boldsymbol{q}}^\top \quad q_4\,]^\top$ is the relative attitude quaternion between the chief and deputy, with $\bar{\boldsymbol{q}} = [\,q_1 \quad q_2 \quad q_3\,]^\top$ and q_4 being the vector and scalar part, respectively. The superscript C indicates that the vector $\boldsymbol{\omega}_C$ is expressed in the chief's BF frame. Then, $\boldsymbol{A}(\boldsymbol{q})$ is the attitude transformation matrix from the chief's BF frame to the deputy's BF frame, given by [23]

$$\boldsymbol{A}(\boldsymbol{q}) = \begin{bmatrix} q_1^2 - q_2^2 - q_3^2 + q_4^2 & 2(q_1q_2 + q_3q_4) & 2(q_1q_3 - q_2q_4) \\ 2(q_1q_2 - q_3q_4) & -q_1^2 + q_2^2 - q_3^2 + q_4^2 & 2(q_2q_3 + q_1q_4) \\ 2(q_1q_3 + q_2q_4) & 2(q_2q_3 - q_1q_4) & -q_1^2 - q_2^2 + q_3^2 + q_4^2 \end{bmatrix} \qquad (2)$$

By assuming that both the chief and deputy spacecraft are rigid bodies, then the attitude dynamics of the deputy can be represented as

$$\dot{\boldsymbol{\omega}}_D = -\boldsymbol{J}_D^{-1}\boldsymbol{\omega}_D^\times(\boldsymbol{J}_D\boldsymbol{\omega}_D) + \boldsymbol{J}_D^{-1}(\boldsymbol{\tau}_L + \boldsymbol{\tau}_M + \boldsymbol{\tau}_G + \boldsymbol{\tau}_P) \qquad (3)$$

where $\boldsymbol{J}_D \in \mathbb{R}^{3\times3}$ is the inertia matrix of the deputy, and $\boldsymbol{\tau}_L, \boldsymbol{\tau}_M, \boldsymbol{\tau}_G$, and $\boldsymbol{\tau}_P$ are, respectively, the Lorentz torque, magnetic torque, gravity gradient torque, and external perturbative torque acting on the deputy. Also, $\boldsymbol{\tau}_G = 3\mu\boldsymbol{R}_D^\times(\boldsymbol{J}_D\boldsymbol{R}_D)/\|\boldsymbol{R}_D\|^5$, where μ is the gravitational parameter of Earth [19]. For a vector $\boldsymbol{a} = [\,a_x \quad a_y \quad a_z\,]^\top$, $\boldsymbol{a}^\times$ denotes a cross-product matrix, given by

$$\boldsymbol{a}^\times = \begin{bmatrix} 0 & -a_z & a_y \\ a_z & 0 & -a_x \\ -a_y & a_x & 0 \end{bmatrix} \qquad (4)$$

In view of Eq. (1) and $\dot{\boldsymbol{A}}(\boldsymbol{q}) = -\boldsymbol{\omega}^\times\boldsymbol{A}(\boldsymbol{q})$, the relative attitude dynamics of the deputy with respect to the chief can be rewritten as

$$\begin{cases} \dot{\boldsymbol{q}} = (1/2)\boldsymbol{\Xi}(\boldsymbol{q})\boldsymbol{\omega} \\ \dot{\boldsymbol{\omega}} = \boldsymbol{\omega}^\times\boldsymbol{\omega}_C - \boldsymbol{A}(\boldsymbol{q})(\dot{\boldsymbol{\omega}}_C|_C)^C - \boldsymbol{J}_D^{-1}(\boldsymbol{\omega} + \boldsymbol{\omega}_C)^\times\boldsymbol{J}_D(\boldsymbol{\omega} + \boldsymbol{\omega}_C) \\ \quad + \boldsymbol{J}_D^{-1}(\boldsymbol{\tau}_L + \boldsymbol{\tau}_M + \boldsymbol{\tau}_G + \boldsymbol{\tau}_P) \end{cases} \qquad (5)$$

with

$$\boldsymbol{\Xi}(\boldsymbol{q}) = \begin{bmatrix} q_4\boldsymbol{I}_{3\times3} + \bar{\boldsymbol{q}}^\times \\ -\bar{\boldsymbol{q}}^\top \end{bmatrix} \qquad (6)$$

where $\boldsymbol{I}_{3\times3}$ is a 3×3 identity matrix.

The orbit dynamics of the chief and deputy are, respectively, governed by

$$\ddot{\boldsymbol{R}}_C|_I = -\frac{\mu}{\|\boldsymbol{R}_C\|^3}\boldsymbol{R}_C + \boldsymbol{a}_{P,C} \qquad (7)$$

and

$$\ddot{\boldsymbol{R}}_D|_I = -\frac{\mu}{\|\boldsymbol{R}_D\|^3}\boldsymbol{R}_D + \boldsymbol{a}_L + \boldsymbol{a}_T + \boldsymbol{a}_{P,D} \qquad (8)$$

where $\boldsymbol{a}_{P,C}$ is the external perturbation experienced by the chaser. Also, $\boldsymbol{a}_L$, $\boldsymbol{a}_T$, and $\boldsymbol{a}_{P,D}$ are, respectively, the Lorentz acceleration, thruster-generated control acceleration, and external perturbations acting on the deputy.

Define $\boldsymbol{\rho} = \boldsymbol{R}_D - \boldsymbol{R}_C = [\,x \quad y \quad z\,]^\top$ as the relative position vector, and $\dot{\boldsymbol{\rho}} = [\,\dot{x} \quad \dot{y} \quad \dot{z}\,]^\top$ as the relative velocity vector. Notably, $\boldsymbol{\omega}_D$ is the rotational velocity of the BF frame with respect to the ECI frame, then it holds that

$$\dot{\boldsymbol{\rho}}|_I = \dot{\boldsymbol{\rho}} + \boldsymbol{\omega}_D^\times\boldsymbol{\rho} \qquad (9)$$

and

$$\ddot{\boldsymbol{\rho}}|_I = \ddot{\boldsymbol{\rho}} + \dot{\boldsymbol{\omega}}_D^\times\boldsymbol{\rho} + 2\boldsymbol{\omega}_D^\times\dot{\boldsymbol{\rho}} + \boldsymbol{\omega}_D^{\times2}\boldsymbol{\rho} \qquad (10)$$

where $\dot{\boldsymbol{\rho}}|_I$ is the absolute derivative, and $\dot{\boldsymbol{\rho}}$ is the relative derivative.

In view of Eqs. (7) and (8), it holds that $\ddot{\boldsymbol{\rho}}|_I = \ddot{\boldsymbol{R}}_D|_I - \ddot{\boldsymbol{R}}_C|_I$. Substitution of it into Eq. (10) yields the equation of relative orbit dynamics expressed in the BF frame, given by

$$\ddot{\boldsymbol{\rho}} = -\dot{\boldsymbol{\omega}}_D^\times\boldsymbol{\rho} - 2\boldsymbol{\omega}_D^\times\dot{\boldsymbol{\rho}} - \boldsymbol{\omega}_D^{\times2}\boldsymbol{\rho} - n_D^2(\boldsymbol{R}_C + \boldsymbol{\rho}) + n_C^2\boldsymbol{R}_C + \boldsymbol{a}_L + \boldsymbol{a}_T + \Delta\boldsymbol{a}_P \qquad (11)$$

where $n_C^2 = \mu/\|\boldsymbol{R}_C\|^3$ and $n_D^2 = \mu/\|\boldsymbol{R}_D\|^3$. Also, $\Delta\boldsymbol{a}_P = \boldsymbol{a}_{P,D} - \boldsymbol{a}_{P,C}$ is the differential external perturbations.

Heretofore, the equations of relative attitude and orbit motion have been derived as Eqs. (5) and (11), respectively.

B. Lorentz Acceleration

The charged deputy spacecraft moving in the magnetic field is subject to the Lorentz acceleration, given by [9]

$$\boldsymbol{a}_L = m^{-1}\sum_{i=1}^{6}\boldsymbol{F}_{Li} = m^{-1}\sum_{i=1}^{6}Q_i\boldsymbol{V}_{ri}^\times\boldsymbol{B}_i = m^{-1}\sum_{i=1}^{6}Q_i\boldsymbol{l}_i \qquad (12)$$

where $\boldsymbol{l}_i = \boldsymbol{V}_{ri}^\times\boldsymbol{B}_i$. Also, m is the mass of the deputy spacecraft, Q_i is the net charge of the ith Coulomb shell, and $\boldsymbol{B}_i$ is the magnetic field local at the ith Coulomb shell. $\boldsymbol{V}_{ri}$ is the velocity of the ith Coulomb shell with respect to the local magnetic field, given by

$$\boldsymbol{V}_{ri} = \dot{\boldsymbol{R}}_i|_I - \boldsymbol{\omega}_E^\times\boldsymbol{R}_i = \dot{\boldsymbol{R}}_D|_I + \dot{\boldsymbol{r}}_i|_I - \boldsymbol{\omega}_E^\times\boldsymbol{R}_i \qquad (13)$$

where $\boldsymbol{\omega}_E$ is the angular velocity vector of Earth.

Notably, the position of the ith Coulomb shell (i.e., $\boldsymbol{r}_i$) remains constant in the BF frame, indicating that $\dot{\boldsymbol{r}}_i = \boldsymbol{0}$. Then, given that $\dot{\boldsymbol{r}}_i|_I = \dot{\boldsymbol{r}}_i + \boldsymbol{\omega}_D^\times\boldsymbol{r}_i$, Eq. (13) reduces to

$$\boldsymbol{V}_{ri} = \dot{\boldsymbol{R}}_D|_I + \boldsymbol{\omega}_D^\times\boldsymbol{r}_i - \boldsymbol{\omega}_E^\times(\boldsymbol{R}_D + \boldsymbol{r}_i) \qquad (14)$$

Obviously, the size of the deputy spacecraft is negligibly small as compared with the orbital radius of the deputy spacecraft (i.e., $\|\boldsymbol{r}_i\| \ll \|\boldsymbol{R}_D\|$) [22]. Also, the entangling velocity is negligibly small as compared with the orbit velocity of the deputy spacecraft

(i.e., $\|\boldsymbol{\omega}_D^\times \boldsymbol{r}_i\| \ll \|\dot{\boldsymbol{R}}_D|_I\|$) [22]. Then, it is reasonable to assume that the relative velocity of the ith Coulomb shell can be approximated by that of the c.m. of the deputy spacecraft, given by

$$V_{ri} \approx V_{rD} = \dot{\boldsymbol{R}}_D|_I - \boldsymbol{\omega}_E^\times \boldsymbol{R}_D = \dot{\boldsymbol{R}}_D + (\boldsymbol{\omega}_D - \boldsymbol{\omega}_E)^\times \boldsymbol{R}_D \quad (15)$$

Meanwhile, for a typical LEO, if the relative distance is within 10 km, the corresponding relative error of the magnitude of the magnetic field is less than 0.5%, and the relative error of the direction of the magnetic field is no more than 0.3° [12]. Thus, in view of the size of the spacecraft, the magnetic field at the c.m. of the ith Coulomb shell (i.e., $\boldsymbol{B}_i$) can be approximated by that at the c.m. of the deputy spacecraft (i.e., $\boldsymbol{B}_D$); that is, $\boldsymbol{B}_i \approx \boldsymbol{B}_D$.

Then, in combination of the aforementioned approximations on the relative velocity and the magnetic field, the total Lorentz acceleration acting on the deputy can thus be approximated by

$$\boldsymbol{a}_L \approx \hat{\boldsymbol{a}}_L = m^{-1} \sum_{i=1}^{6} Q_i V_{rD}^\times \boldsymbol{B}_D = m^{-1} \sum_{i=1}^{6} Q_i \boldsymbol{l} = m^{-1} Q_D \boldsymbol{l} \quad (16)$$

where $\boldsymbol{l} = V_{rD}^\times \boldsymbol{B}_D$, and $Q_D = \sum_{i=1}^{6} Q_i$ is the total net charge of the deputy spacecraft. Correspondingly, the approximation error of the Lorentz acceleration can thus be derived as

$$\Delta \boldsymbol{a}_L = \boldsymbol{a}_L - \hat{\boldsymbol{a}}_L \quad (17)$$

C. Lorentz Torque

Because of the displacement of the Coulomb shells, the resulting Lorentz torque at the c.m. of the deputy is given by [14]

$$\boldsymbol{\tau}_L = \sum_{i=1}^{6} \boldsymbol{r}_i^\times \boldsymbol{F}_{Li} = \sum_{i=1}^{6} Q_i \boldsymbol{r}_i^\times \boldsymbol{l}_i \quad (18)$$

where $\boldsymbol{F}_{Li} = Q_i \boldsymbol{l}_i$ is the Lorentz force acting on the ith Coulomb shell.

Similarly, in view of the approximations on the relative velocity and magnetic field, the Lorentz torque can be approximated by

$$\boldsymbol{\tau}_L \approx \hat{\boldsymbol{\tau}}_L = \sum_{i=1}^{6} Q_i \boldsymbol{r}_i^\times \boldsymbol{l} \quad (19)$$

To further simplify the expression of the Lorentz torque, it is assumed here that the six Coulomb shells are installed asymmetrically along each axis, that is,

$$\begin{cases} \boldsymbol{r}_1 = -\boldsymbol{r}_2 = r_x \boldsymbol{x}^0 \\ \boldsymbol{r}_3 = -\boldsymbol{r}_4 = r_y \boldsymbol{y}^0 \\ \boldsymbol{r}_5 = -\boldsymbol{r}_6 = r_z \boldsymbol{z}^0 \end{cases} \quad (20)$$

where the superscript 0 denotes a unit vector in that direction. Then, the Lorentz torque $\hat{\boldsymbol{\tau}}_L$ further reduces to

$$\hat{\boldsymbol{\tau}}_L = \boldsymbol{m}_L^\times \boldsymbol{l} \quad (21)$$

with

$$\boldsymbol{m}_L = \boldsymbol{\Gamma}\Delta\boldsymbol{Q} = [(Q_1 - Q_2)r_x \ (Q_3 - Q_4)r_y \ (Q_5 - Q_6)r_z]^\top \quad (22)$$

where $\boldsymbol{\Gamma} = \mathrm{diag}(r_x, r_y, r_z) \in \mathbb{R}^{3\times3}$ ($r_j > 0, j = x, y, z$) is a diagonal positive-definite matrix, and the differential charge vector is $\Delta\boldsymbol{Q} = [(Q_1 - Q_2) \ (Q_3 - Q_4) \ (Q_5 - Q_6)]^\top \in \mathbb{R}^3$. Obviously, it holds that $\Delta\boldsymbol{Q} = \boldsymbol{\Gamma}^{-1}\boldsymbol{m}_L$.

Also, the approximation error of the Lorentz torque is thus derived as

$$\Delta\boldsymbol{\tau}_L = \boldsymbol{\tau}_L - \hat{\boldsymbol{\tau}}_L \quad (23)$$

D. Magnetic Torque

The magnetic torques are generated by the three orthogonal magnetic coils, given by [24]

$$\boldsymbol{\tau}_M = \boldsymbol{m}_M^\times \boldsymbol{B}_D \quad (24)$$

where $\boldsymbol{m}_M$ refers to the magnetic dipole moments of the three coils.

III. Closed-Loop Control Scheme

A. Error Dynamic Model

Define the desired relative attitude quaternion and angular velocity as $\boldsymbol{q}_d = [\bar{\boldsymbol{q}}_d^\top \ q_{d4}]^\top$ and $\boldsymbol{\omega}_d$, respectively. Then, the relative attitude quaternion error can be derived as $\boldsymbol{q}_e = [\bar{\boldsymbol{q}}_e^\top \ q_{e4}]^\top = \boldsymbol{q}_d^{-1} \circ \boldsymbol{q}$, where $\boldsymbol{q}_d^{-1} = [-\bar{\boldsymbol{q}}_d^\top \ q_{d4}]^\top$ is the inverse of the quaternion, and the operator $\circ$ denotes the quaternion multiplication. The relative angular velocity error can then be derived as

$$\boldsymbol{\omega}_e = \boldsymbol{\omega} - A(\boldsymbol{q}_e)\boldsymbol{\omega}_d^d \quad (25)$$

where the superscript d denotes the desired BF frame.

Note that $\dot{A}(\boldsymbol{q}_e) = -\boldsymbol{\omega}_e^\times A(\boldsymbol{q}_e)$, then taking the time derivative of Eq. (25) yields the equation of error relative attitude dynamics in the BF frame, given by

$$\begin{cases} \dot{\boldsymbol{q}}_e = (1/2)\boldsymbol{\Xi}(\boldsymbol{q}_e)\boldsymbol{\omega}_e \\ \dot{\boldsymbol{\omega}}_e = \boldsymbol{f}_a + \boldsymbol{J}_D^{-1}(\hat{\boldsymbol{\tau}}_L + \boldsymbol{\tau}_M + \boldsymbol{\tau}_G + \boldsymbol{\tau}_t) \end{cases} \quad (26)$$

with

$$\boldsymbol{f}_a = \boldsymbol{\omega}^\times \boldsymbol{\omega}_C - A(\boldsymbol{q})(\dot{\boldsymbol{\omega}}_C|_C)^C - \boldsymbol{J}_D^{-1}(\boldsymbol{\omega} + \boldsymbol{\omega}_C)^\times \boldsymbol{J}_D(\boldsymbol{\omega} + \boldsymbol{\omega}_C)$$
$$+ \boldsymbol{\omega}_e^\times A(\boldsymbol{q}_e)\boldsymbol{\omega}_d^d - A(\boldsymbol{q}_e)(\dot{\boldsymbol{\omega}}_d|_d)^d \quad (27)$$

where $\boldsymbol{\tau}_t = \boldsymbol{\tau}_P + \Delta\boldsymbol{\tau}_L$ is the total disturbances consisting of the external perturbations and approximation errors. Notably, the upper bound of $\boldsymbol{\tau}_t$ is unknown; that is, $\|\boldsymbol{\tau}_t\| < \tau_{tM}$ and $\tau_{tM} > 0$.

Then, define the desired relative position as $\boldsymbol{\rho}_d$, and the relative position error is derived as $\boldsymbol{\rho}_e = \boldsymbol{\rho} - A(\boldsymbol{q}_e)\boldsymbol{\rho}_d^d$. Similarly, taking the second-order time derivative of $\boldsymbol{\rho}_e$ yields the equation of error relative orbit dynamics in the BF frame, given by

$$\ddot{\boldsymbol{\rho}}_e = \dot{\boldsymbol{\omega}}_e^\times A(\boldsymbol{q}_e)\boldsymbol{\rho}_d^d - \boldsymbol{\omega}_e^{\times2} A(\boldsymbol{q}_e)\boldsymbol{\rho}_d^d + 2\boldsymbol{\omega}_e^\times A(\boldsymbol{q}_e)(\dot{\boldsymbol{\rho}}_d|_d)^d$$
$$- A(\boldsymbol{q}_e)(\ddot{\boldsymbol{\rho}}_d|_d)^d - \dot{\boldsymbol{\omega}}_D^\times \boldsymbol{\rho} - 2\boldsymbol{\omega}_D^\times \dot{\boldsymbol{\rho}} - \boldsymbol{\omega}_D^{\times2}\boldsymbol{\rho} - n_D^2(\boldsymbol{R}_C + \boldsymbol{\rho})$$
$$+ n_C^2 \boldsymbol{R}_C + \hat{\boldsymbol{a}}_L + \boldsymbol{a}_T + \boldsymbol{a}_t \quad (28)$$

where $\boldsymbol{a}_t = \Delta\boldsymbol{a}_P + \Delta\boldsymbol{a}_L$ is the total disturbances consisting of the differential external perturbations and approximation errors. Similarly, the upper bound of $\boldsymbol{a}_t$ is also unknown, satisfying $\|\boldsymbol{a}_t\| < a_{tM}$ and $a_{tM} > 0$.

In view of the expressions of $\dot{\boldsymbol{\omega}}_D$ and $\dot{\boldsymbol{\omega}}_e$ in Eqs. (3) and (26), due to the unknown external perturbations $\boldsymbol{\tau}_P$, $\dot{\boldsymbol{\omega}}_D$ and $\dot{\boldsymbol{\omega}}_e$ are also unknown and cannot be used directly for feedback control. To solve this problem, a pseudo-relative velocity error vector (i.e., $\boldsymbol{v}_e$) is defined as

$$\boldsymbol{v}_e = \dot{\boldsymbol{\rho}}_e + \boldsymbol{\omega}_e^\times \boldsymbol{\rho}_e$$
$$= \dot{\boldsymbol{\rho}} + \boldsymbol{\omega}_e^\times A(\boldsymbol{q}_e)\boldsymbol{\rho}_d^d - A(\boldsymbol{q}_e)(\dot{\boldsymbol{\rho}}_d|_d)^d + \boldsymbol{\omega}_e^\times \boldsymbol{\rho}_e \quad (29)$$

Then, in view of Eq. (11), taking the time derivative of $\boldsymbol{v}_e$ yields that

$$\dot{v}_e = \ddot{\rho} + \dot{\omega}_e^\times A(q_e)\rho_d^d + \omega_e^\times \dot{A}(q_e)\rho_d^d + \omega_e^\times A(q_e)(\dot{\rho}_d|_d)^d$$
$$\quad - \dot{A}(q_e)(\dot{\rho}_d|_d)^d - A(q_e)(\ddot{\rho}_d|_d)^d + \dot{\omega}_e^\times \rho_e + \omega_e^\times \dot{\rho}_e$$
$$= -\dot{\omega}_D^\times \rho - 2\omega_D^\times \dot{\rho} - \omega_D^{\times 2}\rho - n_D^2(R_C + \rho) + n_C^2 R_C + \hat{a}_L + a_T$$
$$\quad + a_t + \dot{\omega}_e^\times[A(q_e)\rho_d^d + \rho_e] - \omega_e^{\times 2}A(q_e)\rho_d^d + 2\omega_e^\times A(q_e)(\dot{\rho}_d|_d)^d$$
$$\quad - A(q_e)(\ddot{\rho}_d|_d)^d + \omega_e^\times \dot{\rho}_e$$
$$= (-\dot{\omega}_D^\times + \dot{\omega}_e^\times)\rho - 2\omega_D^\times \dot{\rho} - \omega_D^{\times 2}\rho - n_D^2(R_C + \rho) + n_C^2 R_C$$
$$\quad - \omega_e^{\times 2}A(q_e)\rho_d^d + 2\omega_e^\times A(q_e)(\dot{\rho}_d|_d)^d - A(q_e)(\ddot{\rho}_d|_d)^d$$
$$\quad + \omega_e^\times \dot{\rho}_e + \hat{a}_L + a_T + a_t \tag{30}$$

Given that $\omega_D = \omega + A(q)\omega_C^C = \omega_e + A(q_e)\omega_d^d + A(q)\omega_C^C$, the time derivative of ω_D is derived as

$$\dot{\omega}_D = \dot{\omega}_e + \dot{A}(q_e)\omega_d^d + A(q_e)(\dot{\omega}_d|_d)^d + \dot{A}(q)\omega_C^C + A(q)(\dot{\omega}_C|_C)^C$$
$$= \dot{\omega}_e - \omega_e^\times A(q_e)\omega_d^d + A(q_e)(\dot{\omega}_d|_d)^d - \omega^\times A(q)\omega_C^C$$
$$\quad + A(q)(\dot{\omega}_C|_C)^C \tag{31}$$

Substitution of Eq. (31) into Eq. (30) yields that

$$\dot{v}_e = f_\rho + \hat{a}_L + a_T + a_t \tag{32}$$

where

$$f_\rho = [\omega_e^\times A(q_e)\omega_d^d - A(q_e)(\dot{\omega}_d|_d)^d + \omega^\times A(q)\omega_C^C - A(q)(\dot{\omega}_C|_C)^C]^\times \rho$$
$$\quad - 2\omega_D^\times \dot{\rho} - \omega_D^{\times 2}\rho - n_D^2(R_C + \rho) + n_C^2 R_C - \omega_e^{\times 2}A(q_e)\rho_d^d$$
$$\quad + 2\omega_e^\times A(q_e)(\dot{\rho}_d|_d)^d - A(q_e)](\ddot{\rho}_d|_d)^d + \omega_e^\times \dot{\rho}_e \tag{33}$$

As can be seen, by replacement of $\dot{\rho}_e$ with v_e, all variables in f_ρ are known, and can be used for feedback. In this way, the dynamic equations of error relative attitude and orbit motion have now been derived as Eqs. (26) and (32), respectively. Define the error relative state vector as $e = [\bar{q}_e^\top \quad \rho_e^\top \quad \omega_e^\top \quad v_e^\top]^\top$, then the error relative attitude and orbit dynamics can be represented as

$$\dot{e} = F(e) + Gu + Gd \tag{34}$$

with

$$F(e) = \begin{bmatrix} (q_{e4}I_{3\times3} + \bar{q}_e^\times)\omega_e/2 \\ v_e - \omega_e^\times \rho_e \\ f_a + J_D^{-1}\tau_G \\ f_\rho \end{bmatrix}, \quad G = \begin{bmatrix} 0_{3\times3} & 0_{3\times3} \\ 0_{3\times3} & 0_{3\times3} \\ J_D^{-1} & 0_{3\times3} \\ 0_{3\times3} & I_{3\times3} \end{bmatrix} \tag{35}$$

where $u = [\tau_D^\top \quad a_D^\top]^\top$ is the control input vector, $\tau_D = \hat{\tau}_L + \tau_M$ is the hybrid control torque composed of the Lorentz torque and magnetic torque, and $a_D = \hat{a}_L + a_T$ is the hybrid control acceleration composed of the Lorentz acceleration and thruster-generated control acceleration. Also, $d = [\tau_t^\top \quad a_t^\top]^\top$ is the total disturbance vector.

Heretofore, the control objective can be summarized as eliminating the initial system states errors and thereafter tracking the desired system states (i.e., $e \to 0$) in the presence of external perturbations and approximation errors with unknown upper bounds.

B. Adaptive Backstepping Controller Design

The relative attitude and orbit controllers are designed via backstepping control method separately as follows. To initiate the relative attitude controller design, the change of coordinates is set as [25]

$$\begin{cases} x_{a1} = \bar{q}_e \\ x_{a2} = \omega_e - \alpha_a \end{cases} \tag{36}$$

where α_a is the virtual control to be designed.

Consider a Lyapunov function as

$$V_{a1} = k_{a1}[\bar{q}_e^\top \bar{q}_e + (1 - q_{e4})^2] = 2k_{a1}(1 - q_{e4}) \tag{37}$$

where $k_{a1} > 0$ is a design parameter. It holds that $V_{a1} > 0, \forall \bar{q}_e \neq 0_{3\times1}$ and $q_{e4} \neq 1$.

In view of Eq. (26), taking the time derivative of V_{a1} yields that

$$\dot{V}_{a1} = k_{a1}\bar{q}_e^\top \omega_e = k_{a1}\bar{q}_e^\top(x_{a2} + \alpha_a) \tag{38}$$

To ensure that $\dot{V}_{a1} < 0$ later, the virtual control α_a is firstly designed as

$$\alpha_a = -c_a \bar{q}_e \tag{39}$$

where $c_a > 0$ is a positive design parameter.

Then, consider another Lyapunov function as

$$V_{a2} = (1/2)x_{a2}^\top J_D x_{a2} > 0, \quad \forall x_{a2} \neq 0_{3\times1} \tag{40}$$

Similarly, the time derivative of V_{a2} is derived as

$$\dot{V}_{a2} = x_{a2}^\top J_D \dot{x}_{a2} = x_{a2}^\top J_D(\dot{\omega}_e - \dot{\alpha}_a)$$
$$= x_{a2}^\top J_D[f_a + J_D^{-1}(\tau_D + \tau_G + \tau_d) + c_a \dot{\bar{q}}_e] \tag{41}$$

Also, to ensure that $\dot{V}_{a2} < 0$, the control law τ_D is designed as

$$\tau_D = -\tau_G - J_D f_a - c_a J_D(q_{e4}I_{3\times3} + \bar{q}_e^\times)\omega_e/2 - k_{a1}\bar{q}_e - k_{a2}x_{a2} - \hat{\tau}_t \tag{42}$$

where $k_{a2} > 0$ is also a positive design parameter. Notably, $\hat{\tau}_t$ denotes the estimate of the total disturbance torque τ_t, and the adaptation law of $\hat{\tau}_t$ is designed as

$$\dot{\hat{\tau}}_t = \gamma_a x_{a2} \tag{43}$$

where $\gamma_a > 0$ is also a positive design parameter. Detailed explanations on the adaptation law design will be given in the following stability analysis.

Similar to the relative attitude controller design, the change of coordinates for the relative orbit controller is set as

$$\begin{cases} x_{\rho1} = \rho_e \\ x_{\rho2} = v_e - \alpha_\rho \end{cases} \tag{44}$$

where α_ρ is the virtual control to be designed.

Consider the following Lyapunov function as

$$V_{\rho1} = (1/2)k_{\rho1}x_{\rho1}^\top x_{\rho1} > 0, \quad \forall x_{\rho1} \neq 0_{3\times1} \tag{45}$$

where $k_{\rho1} > 0$ is a positive constant. Taking the time derivative of $V_{\rho1}$ yields that

$$\dot{V}_{\rho1} = k_{\rho1}\rho_e^\top \dot{\rho}_e = k_{\rho1}\rho_e^\top(v_e - \omega_e^\times \rho_e) \tag{46}$$

Note that $\omega_e^\times$ is a skew-symmetric matrix, and it satisfies that $\rho_e^\top \omega_e^\times \rho_e = 0$. Then, $\dot{V}_{\rho1}$ reduces to

$$\dot{V}_{\rho1} = k_{\rho1}\rho_e^\top v_e \tag{47}$$

Similarly, to render $\dot{V}_{\rho1} < 0$, the virtual control α_ρ is designed as

$$\alpha_\rho = -c_\rho \rho_e \tag{48}$$

where $c_\rho > 0$ is a positive design parameter.

Then, consider another Lyapunov function as

$$V_{\rho 2} = (1/2)\boldsymbol{x}_{\rho 2}^{\top}\boldsymbol{x}_{\rho 2} > 0, \quad \forall \, \boldsymbol{x}_{\rho 2} \neq \boldsymbol{0}_{3\times 1} \tag{49}$$

Taking the time derivative of $V_{\rho 2}$ yields that

$$\dot{V}_{\rho 2} = \boldsymbol{x}_{\rho 2}^{\top}\dot{\boldsymbol{x}}_{\rho 2} = \boldsymbol{x}_{\rho 2}^{\top}(\dot{\boldsymbol{v}}_e - \dot{\boldsymbol{\alpha}}_{\rho})$$
$$= \boldsymbol{x}_{\rho 2}^{\top}(\boldsymbol{f}_{\rho} + \boldsymbol{a}_D + \boldsymbol{a}_t + c_{\rho}\dot{\boldsymbol{\rho}}_e) \tag{50}$$

To ensure that $\dot{V}_{\rho 2} < 0$, the relative position control law $\boldsymbol{a}_D$ is designed as

$$\boldsymbol{a}_D = -k_{\rho 1}\boldsymbol{\rho}_e - \boldsymbol{f}_{\rho} - c_{\rho}\dot{\boldsymbol{\rho}}_e - \hat{\boldsymbol{a}}_t - k_{\rho 2}\boldsymbol{x}_{\rho 2} \tag{51}$$

where $k_{\rho 2} > 0$ is a positive design parameter. Also, $\hat{\boldsymbol{a}}_t$ is the estimate of the total disturbance acceleration $\boldsymbol{a}_t$, and the adaptation law is designed as

$$\dot{\hat{\boldsymbol{a}}}_t = \gamma_{\rho}\boldsymbol{x}_{\rho 2} \tag{52}$$

where $\gamma_{\rho} > 0$ is a positive design parameter.

Heretofore, the relative attitude and position control law have been designed as Eqs. (42) and (51), respectively.

C. Optimal Distribution Laws Design

As aforementioned, the required control torque $\boldsymbol{\tau}_D$ is composed of the Lorentz torque $\hat{\boldsymbol{\tau}}_L$ and the magnetic torque $\boldsymbol{\tau}_M$. In view of Eqs. (21) and (24), the hybrid control inputs for relative attitude control are thus composed of the charge of the Coulomb shell Q_i ($i = 1, 2, \ldots, 6$) and the magnetic dipole moments of the coils $\boldsymbol{m}_M$.

Also, the required control acceleration $\boldsymbol{a}_D$ consists of the Lorentz acceleration $\hat{\boldsymbol{a}}_L$ and the thruster-generated control acceleration $\boldsymbol{a}_T$. In view of Eq. (16), the hybrid control inputs for relative orbit control are thus composed of the charge of the Coulomb shell Q_i ($i = 1, 2, \ldots, 6$) and the thruster-generated control acceleration $\boldsymbol{a}_T$.

Therefore, to fulfill the coupled relative orbit and attitude control, the hybrid control inputs are composed of the charge of the Coulomb shell Q_i ($i = 1, 2, \ldots, 6$), the magnetic dipole moment of the coils $\boldsymbol{m}_M$, and the thruster-generated control acceleration $\boldsymbol{a}_T$. Now, having derived the required control torque $\boldsymbol{\tau}_D$ and acceleration $\boldsymbol{a}_D$ above, it remains to seek the optimal distribution laws of these three control inputs in this subsection, especially the charge of each Coulomb shell Q_i. As can be seen, the charge Q_i should meet both the relative orbit and attitude control requirements simultaneously, which further complicates the optimal distribution laws design.

As depicted in Fig. 2, a plane containing the vectors $\boldsymbol{V}_{rD}$ and $\boldsymbol{B}_D$ is defined as plane $\mathcal{S}$. Given that $\boldsymbol{l} = \boldsymbol{V}_{rD}^{\times}\boldsymbol{B}_D$, $\boldsymbol{l}$ is normal to the plane $\mathcal{S}$. In view of Eq. (21), the Lorentz torque is given by $\hat{\boldsymbol{\tau}}_L = \boldsymbol{m}_L^{\times}\boldsymbol{l}$. Then, it is obvious that $\hat{\boldsymbol{\tau}}_L$ is perpendicular to $\boldsymbol{l}$ and located in the plane $\mathcal{S}$. Similarly, in view of Eq. (24), the magnetic torque is given by $\boldsymbol{\tau}_M = \boldsymbol{m}_M^{\times}\boldsymbol{B}_D$. Then, if the magnetic dipole moments $\boldsymbol{m}_M$ are also designed in plane $\mathcal{S}$, the resulting magnetic torque $\boldsymbol{\tau}_M$ will be normal to plane $\mathcal{S}$ and aligned with the direction of $\boldsymbol{l}$. As can be seen, the Lorentz torque $\hat{\boldsymbol{\tau}}_L$ is in plane $\mathcal{S}$ and the magnetic torque $\boldsymbol{\tau}_M$ is perpendicular to plane $\mathcal{S}$. Notably, given an arbitrary control torque $\boldsymbol{\tau}_D$, it can be decomposed into two components, one in plane $\mathcal{S}$ and another one perpendicular to plane $\mathcal{S}$. Thus, the Lorentz torque $\hat{\boldsymbol{\tau}}_L$ can serve as the component in plane $\mathcal{S}$, and the magnetic torque $\boldsymbol{\tau}_M$ can serve as the component perpendicular to plane $\mathcal{S}$, given by [19]

$$\begin{cases} \hat{\boldsymbol{\tau}}_L = \boldsymbol{\tau}_D - (\boldsymbol{\tau}_D^{\top}\boldsymbol{l}^0)\boldsymbol{l}^0 \\ \boldsymbol{\tau}_M = (\boldsymbol{\tau}_D^{\top}\boldsymbol{l}^0)\boldsymbol{l}^0 \end{cases} \tag{53}$$

In this way, a fully actuated attitude control system driven by the Lorentz and magnetic torques is formed. In other words, as long as $\boldsymbol{l}^0 \neq \boldsymbol{0}$, the Lorentz torque $\hat{\boldsymbol{\tau}}_L$ and magnetic torque $\boldsymbol{\tau}_M$ can compose a control torque $\boldsymbol{\tau}_D$ in an arbitrary direction.
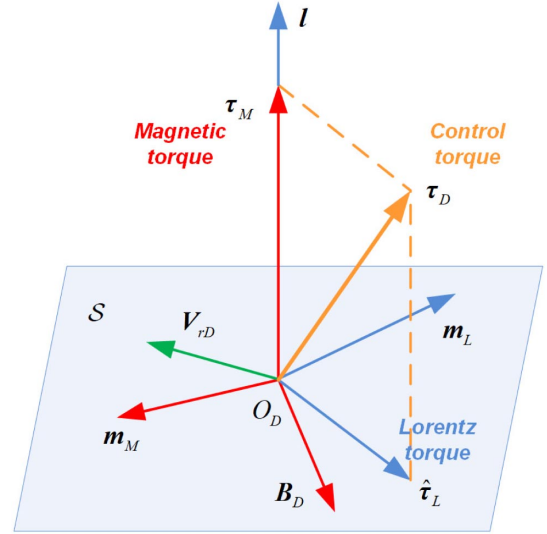

Fig. 2   Decomposition of the control torque.

Having derived the Lorentz torque $\hat{\boldsymbol{\tau}}_L$ and magnetic torque $\boldsymbol{\tau}_M$ necessary for attitude control, the next step is to solve the optimal control inputs consisting of the charge of each Coulomb shell Q_i ($i = 1, 2, \ldots, 6$) and the magnetic dipole moments of the coils $\boldsymbol{m}_M$.

In view of Eqs. (21) and (24), the norms of $\hat{\boldsymbol{\tau}}_L$ and $\boldsymbol{\tau}_M$ are, respectively, derived as

$$\|\hat{\boldsymbol{\tau}}_L\| = \|\boldsymbol{m}_L\| \cdot \|\boldsymbol{l}\| \cdot |\sin\langle \boldsymbol{m}_L, \boldsymbol{l}\rangle| \tag{54}$$

and

$$\|\boldsymbol{\tau}_M\| = \|\boldsymbol{m}_M\| \cdot \|\boldsymbol{B}_D\| \cdot |\sin\langle \boldsymbol{m}_M, \boldsymbol{B}_D\rangle| \tag{55}$$

where $\langle \boldsymbol{a}, \boldsymbol{b}\rangle$ denotes the angle between the vectors $\boldsymbol{a}$ and $\boldsymbol{b}$.

Consider the following objective function as

$$\min J_L = \min \|\boldsymbol{m}_L\| = \min \|\hat{\boldsymbol{\tau}}_L\| \cdot \|\boldsymbol{l}\||^{-1} \cdot |\sin\langle \boldsymbol{m}_L, \boldsymbol{l}\rangle|^{-1} \tag{56}$$

As can be seen, when $\boldsymbol{m}_L$ is perpendicular to $\boldsymbol{l}$ (i.e., $\boldsymbol{m}_L \perp \boldsymbol{l}$), that is, $|\sin\langle \boldsymbol{m}_L, \boldsymbol{l}\rangle| = 1$, the objective function J_L reaches its minimum, given by

$$\|\boldsymbol{m}_L\|^* = \|\hat{\boldsymbol{\tau}}_L\| \cdot \|\boldsymbol{l}\|^{-1} \tag{57}$$

Having derived the optimal norm of $\boldsymbol{m}_L$ (i.e., $\|\boldsymbol{m}_L\|$), it remains to solve the optimal direction of $\boldsymbol{m}_L$ (i.e., $\boldsymbol{m}_L^0$). Notably, given that $\hat{\boldsymbol{\tau}}_L = \boldsymbol{m}_L^{\times}\boldsymbol{l}$, it holds that $\boldsymbol{m}_L \perp \hat{\boldsymbol{\tau}}_L$. As aforementioned, the optimal $\boldsymbol{m}_L$ is also perpendicular to $\boldsymbol{l}$; that is, $\boldsymbol{m}_L \perp \boldsymbol{l}$. Then, the optimal direction $\boldsymbol{m}_L^0$ can be derived as

$$\boldsymbol{m}_L^{0*} = \boldsymbol{l}^{0\times}\hat{\boldsymbol{\tau}}_L^0 \tag{58}$$

Thus, in view of Eqs. (22), (57), and (58), the optimal differential charge vector can be derived as [19]

$$\Delta \boldsymbol{Q}^* = [\Delta Q_x^* \quad \Delta Q_y^* \quad \Delta Q_z^*]^{\top} = \boldsymbol{\Gamma}^{-1}\boldsymbol{m}_L^* = \boldsymbol{\Gamma}^{-1}\|\boldsymbol{m}_L\|^*\boldsymbol{m}_L^{0*}$$
$$= \boldsymbol{\Gamma}^{-1}\|\hat{\boldsymbol{\tau}}_L\| \cdot \|\boldsymbol{l}\|^{-1}(\boldsymbol{l}^{0\times}\hat{\boldsymbol{\tau}}_L^0) \tag{59}$$

Similarly, for the magnetic torque $\boldsymbol{\tau}_M$, consider the following objective function as

$$\min J_M = \min \|\boldsymbol{m}_M\| = \min \|\boldsymbol{\tau}_M\| \cdot \|\boldsymbol{B}_D\||^{-1} \cdot |\sin\langle \boldsymbol{m}_M, \boldsymbol{B}_D\rangle|^{-1} \tag{60}$$

Also, J_M reaches its minimum when $\boldsymbol{m}_M \perp \boldsymbol{B}_D$. Then, by similar methods above, the optimal norm and direction of $\boldsymbol{m}_M$ can be derived as

$$\begin{cases} \|\boldsymbol{m}_M^*\| = \|\boldsymbol{\tau}_M\| \cdot \|\boldsymbol{B}_D\|^{-1} \\ \boldsymbol{m}_M^{0*} = \boldsymbol{B}_D^{0\times} \boldsymbol{\tau}_M^0 \end{cases} \tag{61}$$

Thus, the optimal magnetic dipole moments $\boldsymbol{m}_M^*$ is given by [19]

$$\boldsymbol{m}_M^* = \|\boldsymbol{m}_M\|^* \boldsymbol{m}_M^{0*} = \|\boldsymbol{\tau}_M\| \cdot \|\boldsymbol{B}_D\|^{-1}(\boldsymbol{B}_D^{0\times} \boldsymbol{\tau}_M^0) \tag{62}$$

For relative orbit control, the necessary control acceleration $\boldsymbol{a}_D$ is given by

$$\boldsymbol{a}_D = \hat{\boldsymbol{a}}_L + \boldsymbol{a}_T = m^{-1} Q_D \boldsymbol{l} + \boldsymbol{a}_T \tag{63}$$

Given that chemical fuel is a limited resource onboard, the use of thruster-generated control acceleration $\boldsymbol{a}_T$ should be minimal. Thus, a fuel-optimal objective function is considered here as

$$\min J_F = \min \int_{t_0}^{t_f} L_F \, \mathrm{d}t = \min \int_{t_0}^{t_f} \|\boldsymbol{a}_T\| \, \mathrm{d}t$$
$$= \min \int_{t_0}^{t_f} \|\boldsymbol{a}_D - m^{-1} Q_D \boldsymbol{l}\| \, \mathrm{d}t \tag{64}$$

where t_0 and t_f refer to the initial and final time, respectively.

Solving the following Euler–Lagrange equation

$$\frac{\mathrm{d}}{\mathrm{d}t}\left(\frac{\partial L_F}{\partial \dot{Q}_D}\right) - \frac{\partial L_F}{\partial Q_D} = 0 \tag{65}$$

yields the optimal control inputs necessary for relative orbit control, given by

$$Q_D^* = \begin{cases} (m\boldsymbol{a}_D^\top \boldsymbol{l})/\|\boldsymbol{l}\|^2, & \|\boldsymbol{l}\| \neq \boldsymbol{0} \\ 0, & \|\boldsymbol{l}\| = \boldsymbol{0} \end{cases} \tag{66}$$

and

$$\boldsymbol{a}_T^* = \begin{cases} \boldsymbol{a}_D - (\boldsymbol{a}_D^\top \boldsymbol{l})\boldsymbol{l}/\|\boldsymbol{l}\|^2, & \|\boldsymbol{l}\| \neq \boldsymbol{0} \\ 0, & \|\boldsymbol{l}\| = \boldsymbol{0} \end{cases} \tag{67}$$

As can be seen, to fulfill coupled relative attitude and orbit control simultaneously, the charge of each Coulomb shell Q_i ($i = 1, 2, \ldots, 6$) should satisfy both Eqs. (59) and (66), given by

$$A_Q \boldsymbol{Q} = \boldsymbol{b}_Q \tag{68}$$

with

$$A_Q = \begin{bmatrix} 1 & -1 & 0 & 0 & 0 & 0 \\ 0 & 0 & 1 & -1 & 0 & 0 \\ 0 & 0 & 0 & 0 & 1 & -1 \\ 1 & 1 & 1 & 1 & 1 & 1 \end{bmatrix}, \qquad \boldsymbol{b}_Q = \begin{bmatrix} \Delta Q_x^* \\ \Delta Q_y^* \\ \Delta Q_z^* \\ Q_D^* \end{bmatrix} \tag{69}$$

where $\boldsymbol{Q} = [Q_1 \quad Q_2 \quad \cdots \quad Q_6]^\top \in \mathbb{R}^6$ is the charge vector to be solved.

Notably, in Eq. (68), there are four equations but six unknown variables (i.e., Q_i). The number of unknown variables exceeds that of the equations. Thus, Eq. (68) has infinite solutions. To minimize the consumption of electrical energy, an energy-optimal objective function is considered here as

$$\min J_Q = \min \frac{1}{2} \sum_{i=1}^{6} Q_i^2 = \min \frac{1}{2} \boldsymbol{Q}^\top \boldsymbol{Q} \tag{70}$$

To solve the above optimization problem, a Lagrange function is defined as

$$L_Q = J_Q + \lambda_Q^\top (A_Q \boldsymbol{Q} - \boldsymbol{b}_Q) = \frac{1}{2} \boldsymbol{Q}^\top \boldsymbol{Q} + \lambda_Q^\top (A_Q \boldsymbol{Q} - \boldsymbol{b}_Q) \tag{71}$$

where $\lambda_Q \in \mathbb{R}^4$ is the costate vector.

For optimality conditions, it holds that $\partial L_Q / \partial \boldsymbol{Q} = \boldsymbol{0}_{1\times6}$, given by

$$\boldsymbol{Q}^\top + \lambda_Q^\top A_Q = \boldsymbol{0}_{1\times6} \tag{72}$$

Then, by combination with Eq. (68), it holds that

$$\begin{bmatrix} \boldsymbol{I}_{6\times6} & A_Q^\top \\ A_Q & \boldsymbol{0}_{4\times4} \end{bmatrix} \begin{bmatrix} \boldsymbol{Q} \\ \lambda_Q \end{bmatrix} = \begin{bmatrix} \boldsymbol{0}_{6\times1} \\ \boldsymbol{b}_Q \end{bmatrix} \tag{73}$$

By solving the above equation, the optimal charge vector $\boldsymbol{Q}^*$ is derived as

$$\begin{cases} Q_1^* = (1/6)Q_D^* + (1/2)\Delta Q_x^* \\ Q_2^* = (1/6)Q_D^* - (1/2)\Delta Q_x^* \\ Q_3^* = (1/6)Q_D^* + (1/2)\Delta Q_y^* \\ Q_4^* = (1/6)Q_D^* - (1/2)\Delta Q_y^* \\ Q_5^* = (1/6)Q_D^* + (1/2)\Delta Q_z^* \\ Q_6^* = (1/6)Q_D^* - (1/2)\Delta Q_z^* \end{cases} \tag{74}$$

Heretofore, the optimal control inputs for relative orbit and attitude control (i.e., $\boldsymbol{m}_M^*$, $\boldsymbol{a}_T^*$, and $\boldsymbol{Q}^*$) have been derived as Eqs. (62), (67), and (74), respectively.

Remark 1: Notably, the optimal distribution law of $\Delta \boldsymbol{Q}^*$ in Eq. (59) holds on the precondition that $\boldsymbol{l} \neq \boldsymbol{0}$. The case of $\boldsymbol{l} = \boldsymbol{0}$ has been discussed in detail in [19]. In view of $\boldsymbol{l} = \boldsymbol{V}_{rD}^\times \boldsymbol{B}_D$, $\boldsymbol{l} = \boldsymbol{0}$ holds in the following three cases: $\boldsymbol{V}_{rD} = \boldsymbol{0}$, $\boldsymbol{B}_D = \boldsymbol{0}$, and $\sin\langle \boldsymbol{V}_{rD}, \boldsymbol{B}_D \rangle = 0$. Firstly, the case of $\boldsymbol{V}_{rD} = \boldsymbol{0}$ corresponds to the case that the deputy flies in an ideal two-body geostationary orbit (GEO). Because the geomagnetic field corotates with Earth, the velocity of spacecraft in GEO with respect to the local magnetic field is thus zero. Thus, the optimal distribution laws are infeasible in GEO. Secondly, the case of $\boldsymbol{B}_D = \boldsymbol{0}$ does not hold in geomagnetic field. Finally, the case of $\sin\langle \boldsymbol{V}_{rD}, \boldsymbol{B}_D \rangle = 0$ is the most complicated one, corresponding to the case that the direction of $\boldsymbol{V}_{rD}$ is parallel to that of $\boldsymbol{B}_D$. Numerical simulations in [19] have verified that the direction of $\boldsymbol{V}_{rD}$ is seldom parallel to that of $\boldsymbol{B}_D$, and the precondition $\boldsymbol{l} \neq \boldsymbol{0}$ can be guaranteed for most orbits [19].

Remark 2: Notably, to derive analytical solutions of the optimal charge $\boldsymbol{Q}^*$, this paper fails to consider the input saturation problem. In fact, for actual charge generation devices, there exists an upper bound of the available charge; that is, $|Q_i| \leq Q_m$ ($i = 1, 2, \ldots, 6$), where Q_m refers to the maximum available charge. Without the input saturation constraint, the charge optimization problem is an equality constrained optimization problem that the objective function is Eq. (70), and the equality constraint is Eq. (68). As can be seen, the optimal charge has an analytical solution, as shown in Eq. (74). Differently, in the event of input saturation, the original equality constrained optimization problem turns into an inequality constrained optimization problem. The objective function is still Eq. (70), but the constraints turn into

$$\begin{cases} A_Q \boldsymbol{Q} = \boldsymbol{b}_Q \\ |Q_i| \leq Q_m \end{cases} \tag{75}$$

where $i = 1, 2, \ldots, 6$. Generally, the inequality constrained optimization problem does not have analytical solutions, and can be solved by numerical optimization methods, such as interior-point algorithm and sequence quadratic program algorithm. Given that the main aim of this paper is to obtain the analytical solutions to the optimal charge, the input saturation constraint is temporarily not taken into account in the following numerical simulations. As aforementioned, if the input saturation problem is considered, the optimal numerical solutions can also easily be derived by solving the above inequality constrained optimization problem.

D. Stability Analysis

The block diagram of the closed-loop control system is depicted in Fig. 3, where $X = [\bar{q}^\top \quad \rho^\top \quad \omega^\top \quad \dot{\rho}^\top]^\top$ is the actual state vector, and $X_d = [\bar{q}_d^\top \quad \rho_d^\top \quad \omega_d^\top \quad \dot{\rho}_d^\top]^\top$ is the desired state vector.

The stability analysis of the closed-loop control system is elaborated in the following theorem.

Theorem 1: For the relative attitude and orbit control system in Eqs. (5) and (11), if the control laws are designed as Eqs. (42) and (51), the adaptation laws are designed as Eqs. (43) and (52), and the optimal distribution laws are designed as Eqs. (62), (67), and (74), then the closed-loop system is asymptotically stable.

Proof: Consider the following Lyapunov function as

$$
\begin{aligned}
V &= V_{a1} + V_{a2} + V_{\rho 1} + V_{\rho 2} + (1/2)(\gamma_a^{-1}\tilde{\tau}_t^\top\tilde{\tau}_t + \gamma_\rho^{-1}\tilde{a}_t^\top\tilde{a}_t) \\
\times &= k_{a1}[\bar{q}_e^\top\bar{q}_e + (1 - q_{e4})^2] + (1/2)(x_{a2}^\top J_D x_{a2} + k_{\rho 1}x_{\rho 1}^\top x_{\rho 1} \\
&\quad + x_{\rho 2}^\top x_{\rho 2} + \gamma_a^{-1}\tilde{\tau}_t^\top\tilde{\tau}_t + \gamma_\rho^{-1}\tilde{a}_t^\top\tilde{a}_t)
\end{aligned} \tag{76}
$$

where $\tilde{\tau}_t = \tau_t - \hat{\tau}_t$ is the estimation error of τ_t, and $\tilde{a}_t = a_t - \hat{a}_t$ is the estimation error of a_t.

Obviously, it holds that $V > 0, \forall \bar{q}_e \neq 0, q_{e4} \neq 1, x_{a2} \neq 0, x_{\rho 1} \neq 0, x_{\rho 2} \neq 0, \tilde{\tau}_t \neq 0$, and $\tilde{a}_t \neq 0$.

In view of $\dot{\tilde{\tau}}_t = -\dot{\hat{\tau}}_t$ and $\dot{\tilde{a}}_t = -\dot{\hat{a}}_t$, then taking the time derivative of V yields that

$$
\begin{aligned}
\dot{V} &= -2k_{a1}\dot{q}_{e4} + x_{a2}^\top J_D \dot{x}_{a2} + k_{\rho 1}x_{\rho 1}^\top \dot{x}_{\rho 1} + x_{\rho 2}^\top \dot{x}_{\rho 2} - \gamma_a^{-1}\tilde{\tau}_t^\top\dot{\hat{\tau}}_t - \gamma_\rho^{-1}\tilde{a}_t^\top\dot{\hat{a}}_t \\
&= k_{a1}\bar{q}_e^\top\omega_e + x_{a2}^\top J_D(\dot{\omega}_e - \dot{\alpha}_a) + k_{\rho 1}x_{\rho 1}^\top\dot{\rho}_e + x_{\rho 2}^\top(\dot{v}_e - \dot{\alpha}_\rho) - \tilde{\tau}_t^\top x_{a2} \\
&\quad - \tilde{a}_t^\top x_{\rho 2}
\end{aligned} \tag{77}
$$

Substitution of Eqs. (34), (39), and (48) into Eq. (77) yields that

$$
\begin{aligned}
\dot{V} &= k_{a1}\bar{q}_e^\top\omega_e + x_{a2}^\top J_D(f_a + J_D^{-1}\tau_G + J_D^{-1}\tau_D + J_D^{-1}\tau_t + c_a\dot{\bar{q}}_e) \\
&\quad + k_{\rho 1}x_{\rho 1}^\top(v_e - \omega_e^\times\rho_e) + x_{\rho 2}^\top(f_\rho + a_D + a_t + c_\rho\dot{\rho}_e) - \tilde{\tau}_t^\top x_{a2} - \tilde{a}_t^\top x_{\rho 2}
\end{aligned} \tag{78}
$$

Note that $x_{\rho 1} = \rho_e$ and $x_{\rho 1}^\top\omega_e^\times\rho_e = 0$, then substitution of the control laws Eqs. (42) and (51) into Eq. (78) yields that

$$
\begin{aligned}
\dot{V} &= k_{a1}\bar{q}_e^\top\omega_e + x_{a2}^\top J_D(-k_{a1}J_D^{-1}\bar{q}_e - k_{a2}J_D^{-1}x_{a2} + J_D^{-1}\tilde{\tau}_t) \\
&\quad + k_{\rho 1}x_{\rho 1}^\top v_e + x_{\rho 2}^\top(-k_{\rho 1}\rho_e + \tilde{a}_t - k_{\rho 2}x_{\rho 2}) - \tilde{\tau}_t^\top x_{a2} - \tilde{a}_t^\top x_{\rho 2} \\
&= k_{a1}\bar{q}_e^\top\omega_e - k_{a1}\bar{q}_e^\top(\omega_e - \alpha_a) - k_{a2}x_{a2}^\top x_{a2} + k_{\rho 1}x_{\rho 1}^\top v_e \\
&\quad - k_{\rho 1}\rho_e^\top(v_e - \alpha_\rho) - k_{\rho 2}x_{\rho 2}^\top x_{\rho 2} \\
&= k_{a1}\bar{q}_e^\top\alpha_a - k_{a2}x_{a2}^\top x_{a2} + k_{\rho 1}\rho_e^\top\alpha_\rho - k_{\rho 2}x_{\rho 2}^\top x_{\rho 2} \\
&= -k_{a1}c_a\bar{q}_e^\top\bar{q}_e - k_{a2}x_{a2}^\top x_{a2} - k_{\rho 1}c_\rho\rho_e^\top\rho_e - k_{\rho 2}x_{\rho 2}^\top x_{\rho 2}
\end{aligned} \tag{79}
$$

As can be seen, $\dot{V} < 0, \forall \bar{q}_e \neq 0, x_{a2} \neq 0, \rho_e \neq 0$, and $x_{\rho 2} \neq 0$. It indicates that the error states $\bar{q}_e, x_{a2}, \rho_e$, and $x_{\rho 2}$ will converge to zero asymptotically; that is, $\bar{q}_e \to 0, x_{a2} \to 0, \rho_e \to 0$, and $x_{\rho 2} \to 0$, as $t \to \infty$.

In view of Eq. (36), it holds that $x_{a2} = \omega_e + c_a\bar{q}_e$. Notably, as $t \to \infty$, it holds that $\bar{q}_e \to 0$ and $x_{a2} \to 0$. Then, it can be easily derived that ω_e will also converge to zero asymptotically; that is, $\omega_e \to 0$.

Similarly, in view of Eq. (44), it holds that $x_{\rho 2} = \dot{\rho}_e + \omega_e^\times\rho_e + c_\rho\rho_e$. As aforementioned, when $t \to \infty$, it holds that $x_{\rho 2} \to 0$ and $\rho_e \to 0$. Then, it can also be derived that $\dot{\rho}_e \to 0$, as $t \to \infty$.

Heretofore, it has been substantiated that all state errors (i.e., $\bar{q}_e$, ω_e, ρ_e, and $\dot{\rho}_e$) will converge to zero asymptotically, indicating that the closed-loop system is asymptotically stable. This completes the proof.

IV. Numerical Simulations and Analysis

A. Adaptive Backstepping Controller

A Lorentz-augmented six-DOF spacecraft hovering control mission is simulated here to testify the performance of the proposed control scheme. Spacecraft hovering denotes a relative static state between the chief and deputy spacecraft. To achieve hovering, the deputy spacecraft thrusts continuously to null out the relative acceleration with respect to the chief spacecraft, thus creating an equilibrium state at the desired hovering position ρ_d^L in the LVLH frame [26]. To maintain the hovering configuration, the desired hovering position remains constant in the LVLH frame; that is,

$$
(\dot{\rho}_d|_L)^L = 0_{3\times 1}, \qquad (\ddot{\rho}_d|_L)^L = 0_{3\times 1} \tag{80}
$$

where the superscript L denotes the LVLH frame.

Meanwhile, the deputy's attitude is required to be synchronous with the chief's attitude. Thus, the desired relative attitude quaternion and relative angular velocity are, respectively, given by

$$
q_d = [0 \quad 0 \quad 0 \quad 1]^\top, \qquad \omega_d^d = 0_{3\times 1} \tag{81}
$$

In this example, it is assumed here that the chief's body frame is coincided with the LVLH frame. Thus, for the deputy spacecraft, to keep synchronous with the chief's attitude is to track the LVLH frame's attitude.

The initial time is set as 01 Jan 2019 00:00:00 UTCG. The chief spacecraft is assumed to be flying in a near-circular orbit, and its initial orbital elements are listed in Table 1. Given that J_2 perturbation, arising from the oblateness and nonhomogeneity of Earth, is one of the most dominant perturbations in LEO, it is thus included in the dynamic system as external disturbances. Furthermore, the perturbative torque τ_P is set as $\tau_P = 10^{-7}[\sin(n_0 t) \quad \cos(n_0 t) \quad \cos(n_0 t/2)]^\top$, where $n_0 = \sqrt{\mu/a_C^3}$ is the mean motion of the chief's orbit, with a_C being the semimajor axis of the chief spacecraft.
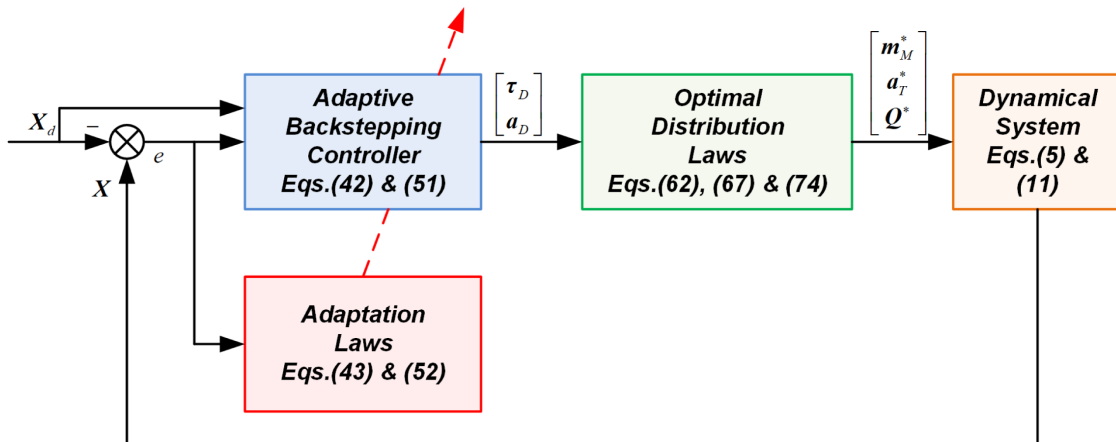

Fig. 3   Block diagram of the closed-loop controller.

**Table 1 Initial orbital elements of the chief spacecraft**

| Orbital element	Value
Semimajor axis, km	6878.137
Eccentricity	0.003
Inclination, deg	42
Right ascension of the ascending node, deg	40
Argument of perigee, deg	0
Argument of latitude, deg	50

The initial relative attitude quaternion is set as $q(0) = [0.128 \quad -0.239 \quad 0.189 \quad 0.944]^T$, corresponding to a pitch angle of 20°, a roll angle of $-30°$, and a yaw angle of 10°. The initial relative angular velocity is set as $\omega(0) = [10^{-3} \quad -2 \times 10^{-3} \quad -5 \times 10^{-4}]^T$ rad/s. The initial relative position and velocity vector are, respectively, set as $\rho(0) = [600 \quad -300 \quad -400]^T$ m and $\dot{\rho}(0) = [-2 \quad 1 \quad 1]^T$ m/s. Also, the desired hovering position is set as $\rho_d^L = [500 \quad 0 \quad 0]^T$ m that the deputy hovers radially above the chief. Other simulation parameters are given in Table 2.

According to the International Geomagnetic Reference Field [12], time histories of the magnetic fields at the deputy's c.m. (i.e., B_D) are depicted in Fig. 4. Notably, without special explanations, the following plots are expressed in the BF frame. Time histories of the relative attitude quaternion errors and relative angular velocity errors are shown in Figs. 5 and 6, respectively. Also, time histories of the relative position and velocity errors are shown in Figs. 7 and 8. Details during the steady process are also enlarged in the figures. As can be seen, all state errors converge to the neighborhood of zero after about half an orbital period. The steady control accuracy of the relative position is on the order of 10^{-1} m, and that of the relative velocity is on the order of 10^{-4} m/s.

Table 2 Simulation parameters

Case	Parameter
Spacecraft	$m = 500$ kg, $J_D = \mathrm{diag}(120, 110, 100)$ kg $\cdot$ m^2, $\Gamma = \mathrm{diag}(10, 10, 10)$ m
ABC	$c_a = 10^{-2}$, $c_\rho = 3 \times 10^{-3}$, $k_{a1} = 5 \times 10^{-3}$, $k_{a2} = 10^{-1}$, $k_{\rho 1} = 4 \times 10^{-5}$, $k_{\rho 2} = 10^{-3}$, $\gamma_a = 10^6$, $\gamma_\rho = 10^8$, $\hat{\tau}_t(0) = 0_{3\times 1}$, $\hat{a}_t(0) = 0_{3\times 1}$
SMC	$\beta_a = 2.13 \times 10^{-2}$, $k_{sa1} = 10^{-3}$, $k_{sa2} = 9 \times 10^{-6}$, $\delta_a = 5 \times 10^{-3}$, $\beta_\rho = 1.48 \times 10^{-2}$, $k_{s\rho 1} = 10^{-3}$, $k_{s\rho 2} = 10^{-6}$, $\delta_\rho = 10^{-2}$
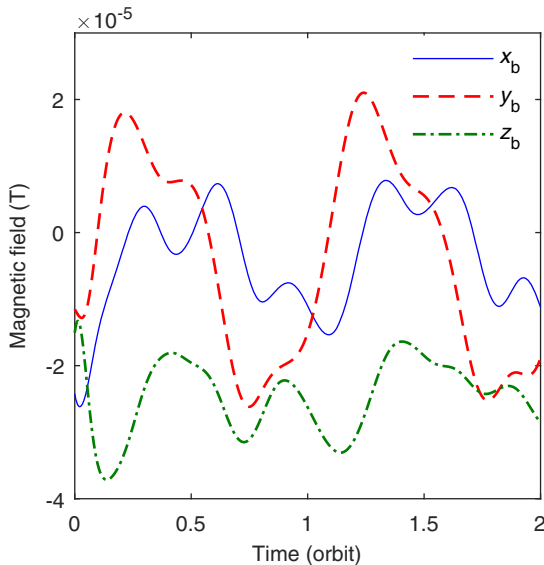
Fig. 4 Time histories of the magnetic fields.
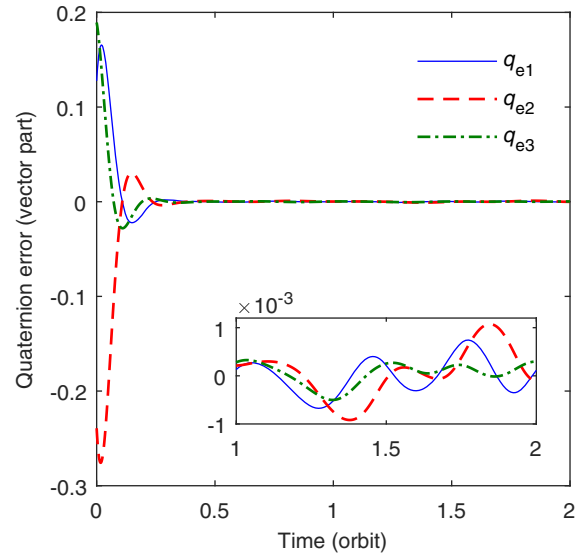
Fig. 5 Time histories of the relative attitude quaternion errors (vector part).
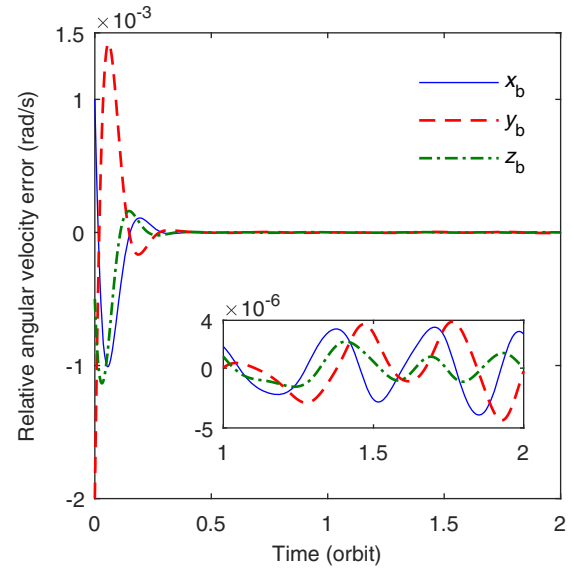
Fig. 6 Time histories of the relative angular velocity errors.
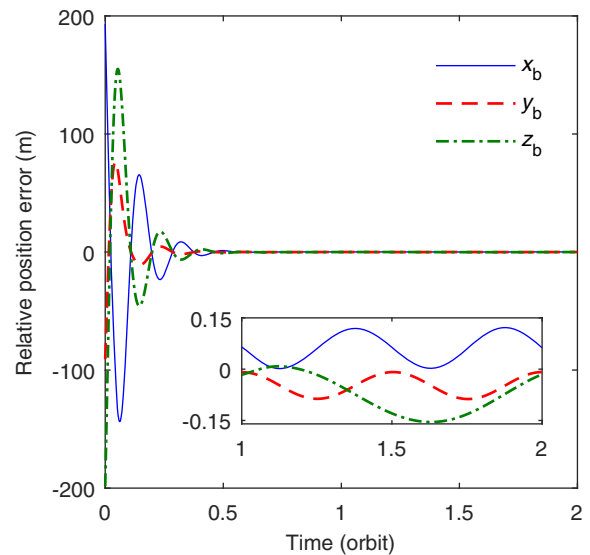
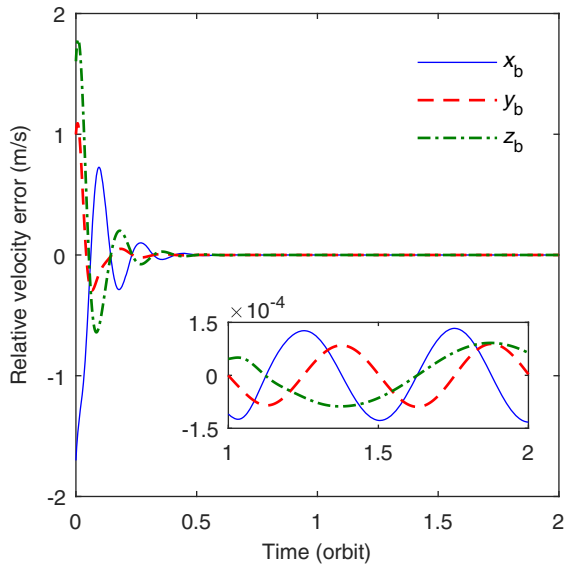**Fig. 7 Time histories of the relative position errors.**

Fig. 8   Time histories of the relative velocity errors.

Fig. 10   Time histories of the thruster-generated control accelerations.

As aforementioned, the hybrid control inputs are composed of the coils' magnetic dipole moments, the thruster-generated control accelerations, and the charges of each Coulomb shell. Figures 9 and 10 give the time histories of the former two kinds of control inputs. Figure 11 gives the time histories of the total charge necessary for relative orbit control (i.e., Q_D), and those of the differential charge necessary for relative attitude control (i.e., ΔQ), as shown in Eq. (69). Also, details during the steady process are enlarged in the right side of the figure. As can be seen, the charging level necessary for relative orbit control is about 10^5 to 10^6 order larger than the charging level for relative attitude control. Then, by using Eq. (74), the optimal charges of each Coulomb shell can be derived, as shown in Fig. 12. Because the magnitude of Q_D is much larger than that of ΔQ, then according to Eq. (74), the optimal charge Q_i ($i = 1, 2, \ldots, 6$) is dominant by Q_D. This explains why the time histories of the charges of each Coulomb shell look similar in Fig. 12. For a Lorentz spacecraft weighting 500 kg, the required charging level corresponds to a specific charge on the order of 10^{-2} C/kg. Notably, it is generally accepted that the near-term feasible charging level of Lorentz spacecraft is about 10^{-3} to 10^{-2} C/kg [17,27]. Thus, the required specific charge is within near-term feasible range.

With the geomagnetic Lorentz forces as primary propulsion, the reduced percent of the consumption of velocity increments can be calculated by
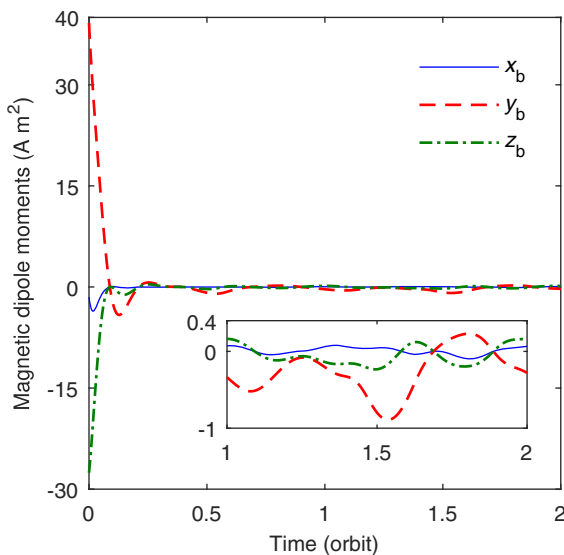
$$\sigma = 1 - \frac{\int_{t_0}^{t_f} \|\boldsymbol{a}_T\| \, dt}{\int_{t_0}^{t_f} \|\boldsymbol{a}_D\| \, dt} \tag{82}$$

which is $\sigma = 71\%$ in this example. As can be seen, by using the optimal distribution laws that minimize the propellant expenditure, the consumption of velocity increments can be greatly reduced, verifying the advantages of Lorentz spacecraft in saving fuels.

Time histories of the estimates of the total perturbative torques and accelerations (i.e., $\hat{\boldsymbol{\tau}}_t$ and $\hat{\boldsymbol{a}}_t$) are, respectively, shown in Figs. 13 and 14. As can be seen, the estimates converge to steady values since about half an orbital period too. Notably, the estimates do not necessarily converge to their true values. Instead, these estimates are only updated and converged for the purpose of closed-loop system stability.

Figure 15 shows the relative transfer trajectory in the LVLH frame. As can be seen, the deputy starts from the initial relative position, and arrives at the final hovering position. Also, three-axis attitude of the BF frame in the LVLH frame is also depicted in Fig. 15. Obviously, the initial attitude deviations have been eliminated, and the final attitude of the BF frame is synchronous with that of the LVLH frame. Heretofore, the validity of the proposed controller has been testified.

Currently, both attitude and orbit controller parameters are chosen by trial and error to guarantee that the control inputs do not exceed their limits. As noted in Remark 2, future research will take the input saturation problem into account, and concentrate on saturated control methods.

B.   Comparisons with Another Controller

To verify the advantages of the proposed adaptive backstepping control scheme, another sliding mode controller (SMC) is introduced to make comparisons. The linear sliding mode surfaces are selected as

$$\begin{cases} \boldsymbol{s}_a = [\, s_{ax} \quad s_{ay} \quad s_{az} \,]^\top = \boldsymbol{\omega}_e + \beta_a \bar{\boldsymbol{q}}_e \\ \boldsymbol{s}_\rho = [\, s_{\rho x} \quad s_{\rho y} \quad s_{\rho z} \,]^\top = \boldsymbol{v}_e + \beta_\rho \boldsymbol{\rho}_e \end{cases} \tag{83}$$

where $\beta_a > 0$ and $\beta_\rho > 0$ are positive design parameters.

Then, the linear sliding mode control laws are designed as

$$\begin{cases} \boldsymbol{\tau}_D = -\boldsymbol{\tau}_G - \boldsymbol{J}_D \big[\beta_a \dot{\bar{\boldsymbol{q}}}_e + \boldsymbol{f}_a + k_{sa1} \boldsymbol{s}_a + k_{sa2} \mathrm{sgn}(\boldsymbol{s}_a) \big] \\ \boldsymbol{a}_D = -\beta_\rho (\boldsymbol{v}_e - \boldsymbol{\omega}_e^\times \boldsymbol{\rho}_e) - \boldsymbol{f}_\rho - k_{s\rho1} \boldsymbol{s}_\rho - k_{s\rho2} \mathrm{sgn}(\boldsymbol{s}_\rho) \end{cases} \tag{84}$$

where sgn denotes the sign function. Also, k_{sa1}, k_{sa2}, $k_{s\rho1}$, and $k_{s\rho2}$ are also positive design constants. It holds that $k_{sa2} > \xi_{tM}$ and $k_{s\rho2} > a_{tM}$, where ξ_{tM} and a_{tM} refer to the upper bound of $\|\boldsymbol{J}_D^{-1} \boldsymbol{\tau}_t\|$
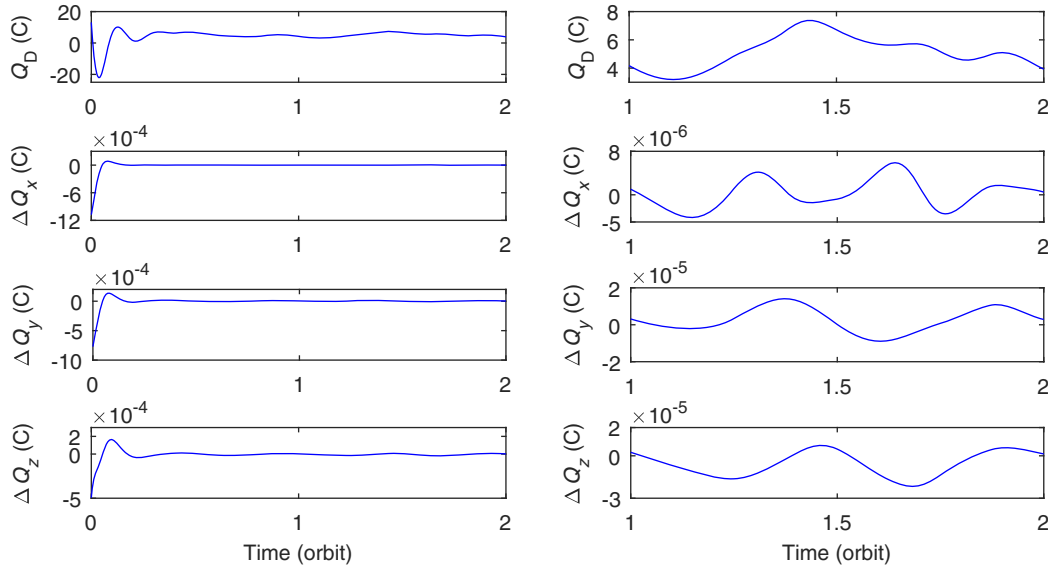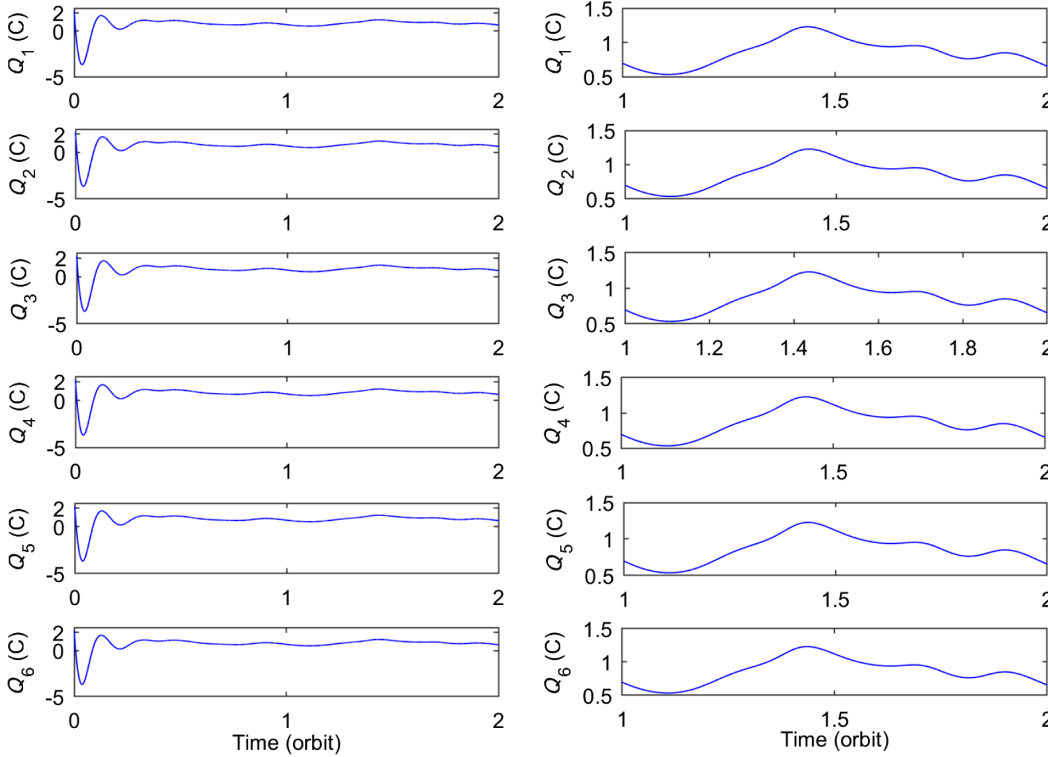

Fig. 9   Time histories of the coils' magnetic dipole moments.

Fig. 11   Time histories of Q_D and ΔQ.

Fig. 12   Time histories of the charges of each Coulomb shell.

and $\|\boldsymbol{a}_t\|$, respectively. Detailed closed-loop system stability analysis is given in the Appendix. Notably, to eliminate the chattering problem arising from the sign functions $\mathrm{sgn}(\boldsymbol{s}_a)$ and $\mathrm{sgn}(\boldsymbol{s}_\rho)$, they are replaced by the saturation functions $\mathrm{sat}(\boldsymbol{s}_a, \delta_a)$ and $\mathrm{sat}(\boldsymbol{s}_\rho, \delta_\rho)$, given by

$$\mathrm{sat}(s_{ai}, \delta_a) = \begin{cases} s_{ai}/\delta_a, & |s_{ai}| < \delta_a \\ \mathrm{sgn}(s_{ai}), & |s_{ai}| \geq \delta_a \end{cases} \qquad (85)$$

and

$$\mathrm{sat}(s_{\rho i}, \delta_\rho) = \begin{cases} s_{\rho i}/\delta_\rho, & |s_{\rho i}| < \delta_\rho \\ \mathrm{sgn}(s_{\rho i}), & |s_{\rho i}| \geq \delta_\rho \end{cases} \qquad (86)$$

where $i = x, y, z$. Also, δ_a and δ_ρ refer to width of the boundary layer, respectively.

The SMC parameters are summarized in Table 2. Notably, to ensure the comparability between the ABC and the SMC, the controller parameters are chosen such that these two controllers consume similar control energy to fulfill the six-DOF hovering control mission. In this way, the comparison results are more justified and reasonable. The energy consumption for orbit control is defined as $J_\rho = (1/2)\int_{t_0}^{t_f} \boldsymbol{a}_D^\top \boldsymbol{a}_D \, \mathrm{d}t$, and the energy expenditure for attitude control is given by $J_a = (1/2)\int_{t_0}^{t_f} \boldsymbol{\tau}_D^\top \boldsymbol{\tau}_D \, \mathrm{d}t$. To quantify the comparison results, the controller performance indices are defined as follows. Define $\|\bar{\boldsymbol{q}}_e\|$ as the norm of the vector part of the error quaternion. The settling time for relative attitude control t_{sa} is defined as the time required by $\|\bar{\boldsymbol{q}}_e\|$ to reach and stay within 1% of the initial value
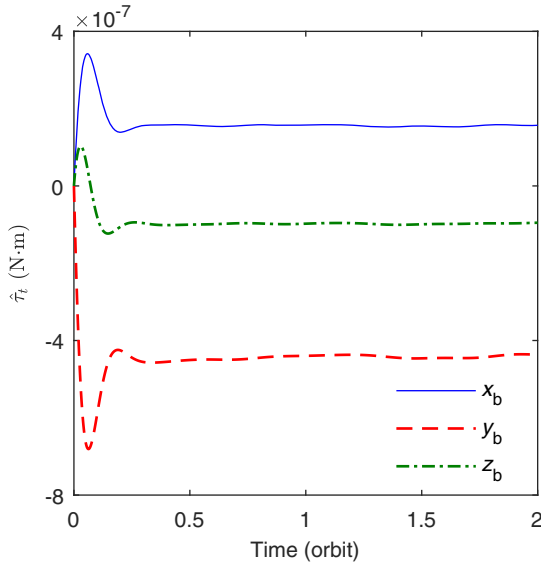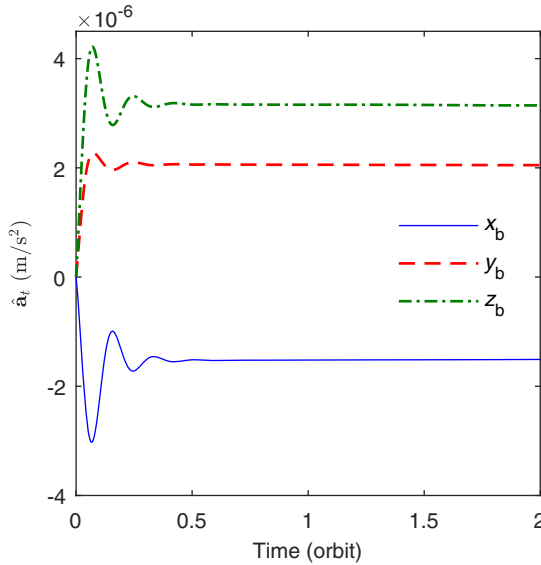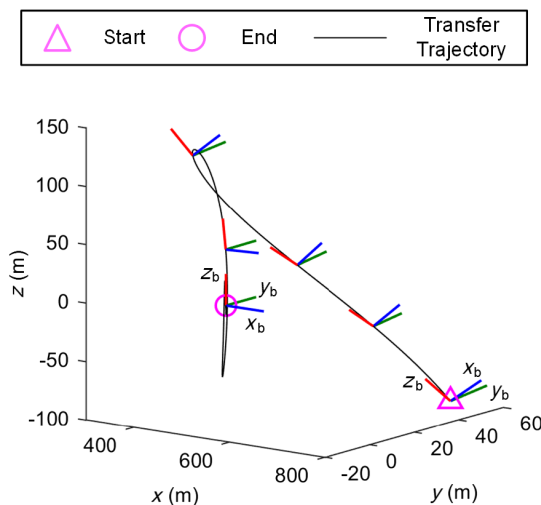
Fig. 13   Time histories of the estimates of $\hat{\tau}_t$.

Fig. 14   Time histories of the estimates of $\hat{a}_t$.

Fig. 15   Transfer trajectory and three-axis attitude of BF frame in LVLH frame.

$\|\bar{q}_e(0)\|$; that is, $\forall t \geq t_{sa}$, $\|\bar{q}_e(t)\| \leq 1\% \|\bar{q}_e(0)\|$. Then, the steady attitude control accuracy e_{sa} is defined as

$$e_{sa} = \underset{t_{sa} \leq t \leq t_f}{\text{mean}} \|\bar{q}_e(t)\| \tag{87}$$

Similarly, define $\|\boldsymbol{\rho}_e\|$ as the norm of the relative position error. The settling time for relative position control $t_{s\rho}$ is defined as the time required by $\|\boldsymbol{\rho}_e\|$ to reach and stay within 1% of the initial value $\|\boldsymbol{\rho}_e(0)\|$; that is, $\forall t \geq t_{s\rho}$, $\|\boldsymbol{\rho}_e(t)\| \leq 1\% \|\boldsymbol{\rho}_e(0)\|$. Likewise, the steady position control accuracy $e_{s\rho}$ is defined as

$$e_{s\rho} = \underset{t_{s\rho} \leq t \leq t_f}{\text{mean}} \|\boldsymbol{\rho}_e(t)\| \tag{88}$$

Time histories of the norms of the relative attitude and position errors (i.e., $\bar{q}_e$ and $\boldsymbol{\rho}_e$) are compared in Fig. 16, and time histories of the norms of the control torques and accelerations (i.e., $\boldsymbol{\tau}_D$ and $\boldsymbol{a}_D$) are compared in Fig. 17. As can be seen, both ABC and SMC can manage six-DOF hovering control in a perturbed environment. The steady control accuracy of the relative attitude quaternion is on the
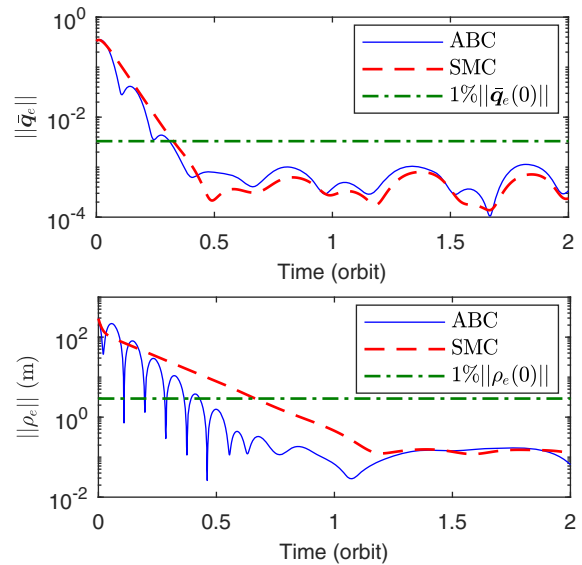

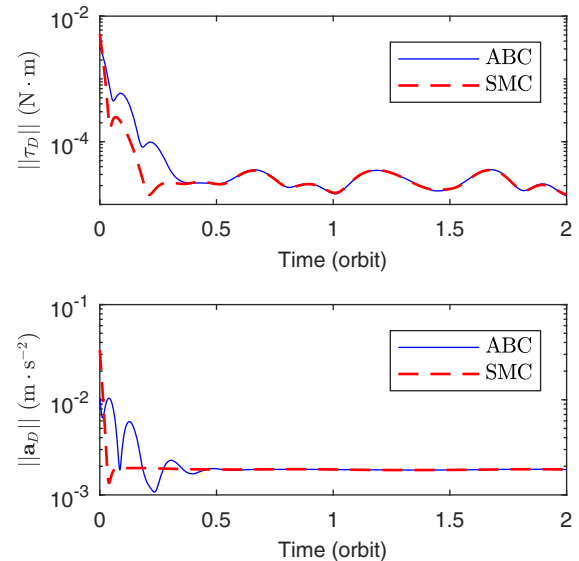**Fig. 16   Time histories of the norms of the state errors.**

Fig. 17   Time histories of the norms of the control torques and accelerations.

Table 3 Performance indices of the controllers

Controller	t_{sa}, orbit	$t_{s\rho}$, orbit	e_{sa}	$e_{s\rho}$, m	J_a, N² · m² · s	J_ρ, m² · s⁻³
			Performance index			
ABC	0.31	0.43	6.79×10^{-4}	2.19×10^{-1}	5.56×10^{-4}	3.76×10^{-2}
SMC	0.33	0.67	4.96×10^{-4}	4.48×10^{-1}	5.56×10^{-4}	3.77×10^{-2}

order of 10^{-4}, and that of the relative position is on the order of 10^{-1} m.

The performance indices of the controllers are summarized in Table 3. At the expense of similar control energy (i.e., J_a and J_ρ), the convergence rate of the ABC is faster than that of the SMC, and the steady relative position error of the ABC is less than half of that of the SMC. In all, except for a bit larger relative attitude error, the performance of the ABC is superior to that of the SMC. Notably, the controller performances vary with different controller parameters, and the comparison results are only valid for this example.

V. Conclusions

This paper investigates the control problem of the coupled relative orbit and attitude motion of Lorentz spacecraft. The difficulties of this problem are mainly attributed to the inherent dynamic coupling and instantaneous underactuation of the Lorentz forces and torques. To render the system fully actuated, auxiliary means of actuation have been introduced. The Lorentz forces, with the thruster-generated control forces as auxiliary propulsion, are used for relative orbit control. The Lorentz torques, in combination with magnetic torques generated by current-driven coils, are used for relative attitude control. In this way, a hybrid control system is developed, and the hybrid control inputs are composed of the charges of the Coulomb shells, the thruster-generated forces, and the magnetic dipole moments of the coils. Based on the dynamic model of coupled relative orbit and attitude motion, a closed-loop control scheme is proposed, including the backstepping control laws, parameter adaptation laws, and optimal distribution laws. The overall stability of the closed-loop system is guaranteed by the Lyapunov-based method. Numerical simulations verify the validity of the proposed control scheme, and the conclusions are as follows:

1) The proposed adaptive backstepping controller can manage six-DOF relative orbit and attitude control augmented by the Lorentz forces and torques, in the presence of unknown external perturbations and model approximation errors.

2) The analytic optimal charging strategy can fulfill the requirements of both relative orbit and attitude control simultaneously.

3) For the relative orbit control system with the Lorentz forces as primary propulsion, the propellant expenditure can be greatly reduced, thus enhancing the maneuvering ability and system lifetime. For the relative attitude control system purely driven by two kinds of electromagnetic torques, no traditional mechanical torques are required, thus providing a novel alternative to spacecraft attitude control.

Appendix: Stability Analysis

The stability analysis of the closed-loop system driven by the SMC is elaborated in the following theorem.*Theorem A1:* For the relative attitude and orbit control system in Eqs. (5) and (11), if the sliding surfaces are designed as Eq. (83), the control laws are designed as Eq. (84), and the optimal distribution laws are designed as Eqs. (62), (67), and (74), then the closed-loop system is asymptotically stable.-*Proof:* Consider the following Lyapunov function as

$$V_s = (1/2)\big(s_a^\top s_a + s_\rho^\top s_\rho\big) \tag{A1}$$

Obviously, it holds that $V_s > 0$, $\forall s_a \neq \mathbf{0}$ and $s_\rho \neq \mathbf{0}$. Taking the time derivative of V_s yields that

$$\dot{V}_s = s_a^\top \dot{s}_a + s_\rho^\top \dot{s}_\rho \tag{A2}$$

Substitution of the sliding surfaces Eq. (83) into Eq. (A2) yields that

$$
\begin{aligned}
\dot{V}_s &= s_a^\top(\dot{\omega}_e + \beta_a \dot{\bar{q}}_e) + s_\rho^\top(\dot{v}_e + \beta_\rho \dot{\rho}_e) \\
&= s_a^\top[f_a + J_D^{-1}(\tau_G + \tau_D + \tau_t) + \beta_a \dot{\bar{q}}_e] \\
&\quad + s_\rho^\top[f_\rho + a_D + a_t + \beta_\rho(v_e - \omega_e^\times \rho_e)]
\end{aligned} \tag{A3}
$$

In view of the control laws in Eq. (84), it holds that

$$
\begin{aligned}
\dot{V}_s &= s_a^\top[-k_{sa1}s_a - k_{sa2}\text{sgn}(s_a) + J_D^{-1}\tau_t] \\
&\quad + s_\rho^\top[-k_{s\rho1}s_\rho - k_{s\rho2}\text{sgn}(s_\rho) + a_t] \\
&\leq -k_{sa1}\|s_a\|^2 - \sum_{i=x,y,z} |s_{ai}|(k_{sa2} - \|J_D^{-1}\tau_t\|) - k_{s\rho1}\|s_\rho\|^2 \\
&\quad - \sum_{i=x,y,z} |s_{\rho i}|(k_{s\rho2} - \|a_t\|)
\end{aligned} \tag{A4}
$$

Given that $k_{sa2} > \xi_{tM}$ and $k_{s\rho2} > a_{tM}$, it holds that $\dot{V}_s < 0$, $\forall s_a \neq \mathbf{0}$ and $s_\rho \neq \mathbf{0}$. It indicates that s_a and s_ρ will converge to zero asymptotically. On the surface of $s_a = \mathbf{0}$, it holds that $\omega_e = -\beta_a \bar{q}_e$. Then, consider another Lyapunov function as $V_a = 2(1 - q_{e4}) > 0$, $\forall q_{e4} \neq 1$. Taking the time derivative of V_a yields that

$$\dot{V}_a = -2\dot{q}_{e4} = \bar{q}_e^\top \omega_e = -\beta_a \bar{q}_e^\top \bar{q}_e \tag{A5}$$

As can be seen, it holds that $\dot{V}_a < 0$, $\forall \bar{q}_e \neq \mathbf{0}$. It indicates that $\bar{q}_e$ will converge to zero asymptotically. In view of $\omega_e = -\beta_a \bar{q}_e$, ω_e will converge to zero asymptotically too. Likewise, on the surface of $s_\rho = \mathbf{0}$, it holds that $\dot{\rho}_e + \omega_e^\times \rho_e + \beta_\rho \rho_e = \mathbf{0}$. Obviously, when $\omega_e \to \mathbf{0}$ as $t \to \infty$, ρ_e and $\dot{\rho}_e$ will also thereafter converge to zero.

Heretofore, it has been substantiated that all state errors (i.e., $\bar{q}_e$, ω_e, ρ_e, and $\dot{\rho}_e$) will converge to zero asymptotically, indicating that the closed-loop system is asymptotically stable. This completes the proof.

References

[1] Harris, A. T., Peterson, C. D., and Schaub, H., "Linear Coupled Attitude–Orbit Control Through Aerodynamic Drag," *Journal of Guidance, Control, and Dynamics*, Vol. 43, No. 1, 2020, pp. 122–131.
https://doi.org/10.2514/1.G004521

[2] Streetman, B., and Peck, M. A., "New Synchronous Orbits Using the Geomagnetic Lorentz Force," *Journal of Guidance, Control, and Dynamics*, Vol. 30, No. 6, 2007, pp. 1677–1690.
https://doi.org/10.2514/1.29080

[3] Forbes, J. R., and Damaren, C. J., "Geometric Approach to Spacecraft Attitude Control Using Magnetic and Mechanical Actuation," *Journal of Guidance, Control, and Dynamics*, Vol. 33, No. 2, 2010, pp. 590–595.
https://doi.org/10.2514/1.46441

[4] Shouman, M., Bando, M., and Hokamoto, S., "Output Regulation Control for Satellite Formation Flying Using Differential Drag," *Journal of Guidance, Control, and Dynamics*, Vol. 42, No. 10, 2019, pp. 2220–2232.
https://doi.org/10.2514/1.G004219

[5] Gangestad, J. W., Pollock, G. E., and Longuski, J. M., "Propellantless Stationkeeping at Enceladus via the Electromagnetic Lorentz Force," *Journal of Guidance, Control, and Dynamics*, Vol. 32, No. 5, 2009, pp. 1466–1475.
https://doi.org/10.2514/1.42769

[6] Cubas, J., Farrahi, A., and Pindado, S., "Magnetic Attitude Control for Satellites in Polar or Sun-Synchronous Orbits," *Journal of Guidance, Control, and Dynamics*, Vol. 38, No. 10, 2015, pp. 1947–1958.
https://doi.org/10.2514/1.G000751

[7] Mason, P., "Prospects and Challenges for Lorentz-Augmented Orbits," *AIAA Guidance, Navigation, and Control Conference and Exhibit*, AIAA Paper 2005-5995, 2005.
https://doi.org/10.2514/6.2005-5995

[8] Mazal, L., Pérez, D., Bevilacqua, R., and Curti, F., "Spacecraft Rendezvous by Differential Drag Under Uncertainties," *Journal of Guidance, Control, and Dynamics*, Vol. 39, No. 8, 2016, pp. 1721–1733.
https://doi.org/10.2514/1.G001785

[9] Pollock, G. E., Gangestad, J. W., and Longuski, J. M., "Analytical Solutions for the Relative Motion of Spacecraft Subject to Lorentz-Force Perturbations," *Acta Astronautica*, Vol. 68, Nos. 1–2, 2011, pp. 204–217.
https://doi.org/10.1016/j.actaastro.2010.07.007

[10] Chocron, S., and Choukroun, D., "Robust Relative Navigation for Spacecraft Rendezvous Using Differential Drag," *Acta Astronautica*, Vol. 158, May 2019, pp. 32–43.
https://doi.org/10.1016/j.actaastro.2018.10.038

[11] Huang, X., Yan, Y., Zhou, Y., and Zhang, H., "Sliding Mode Control for Lorentz-Augmented Spacecraft Hovering Around Elliptic Orbits," *Acta Astronautica*, Vol. 103, Oct. 2014, pp. 257–268.
https://doi.org/10.1016/j.actaastro.2014.07.010

[12] Yan, Y., Huang, X., and Yang, Y., *Dynamics and Control of Lorentz-Augmented Spacecraft Relative Motion*, Springer, Singapore, 2017, Chap. 1.
https://doi.org/10.1007/978-981-10-2603-4

[13] Avanzini, G., and Giulietti, F., "Magnetic Detumbling of a Rigid Spacecraft," *Journal of Guidance, Control, and Dynamics*, Vol. 35, No. 4, 2012, pp. 1326–1334.
https://doi.org/10.2514/1.53074

[14] Giri, D. K., and Sinha, M., "Magnetocoulombic Attitude Control of Earth-Pointing Satellites," *Journal of Guidance, Control, and Dynamics*, Vol. 37, No. 6, 2014, pp. 1946–1960.
https://doi.org/10.2514/1.G000030

[15] Giri, D. K., Sinha, M., and Kumar, K. D., "Fault-Tolerant Attitude Control of Magneto-Coulombic Satellites," *Acta Astronautica*, Vol. 116, Nov. 2015, pp. 254–270.
https://doi.org/10.1016/j.actaastro.2015.06.020

[16] Giri, D. K., and Sinha, M., "Finite-Time Continuous Sliding Mode Magneto-Coulombic Satellite Attitude Control," *IEEE Transactions on Aerospace and Electronic Systems*, Vol. 52, No. 5, 2016, pp. 2397–2412.
https://doi.org/10.1109/TAES.2016.140503

[17] Gangestad, J. W., Pollock, G. E., and Longuski, J. M., "Lagrange's Planetary Equations for the Motion of Electrostatically Charged Spacecraft," *Celestial Mechanics and Dynamical Astronomy*, Vol. 108, No. 2, 2010, pp. 125–145.
https://doi.org/10.1007/s10569-010-9297-z

[18] Sobiesiak, L. A., and Damaren, C. J., "Controllability of Lorentz-Augmented Spacecraft Formations," *Journal of Guidance, Control, and Dynamics*, Vol. 38, No. 11, 2015, pp. 2188–2195.
https://doi.org/10.2514/1.G001148

[19] Huang, X., and Yan, Y., "Fully Actuated Spacecraft Attitude Control via the Hybrid Magnetocoulombic and Magnetic Torques," *Journal of Guidance, Control, and Dynamics*, Vol. 40, No. 12, 2017, pp. 3358–3360.
https://doi.org/10.2514/1.G002925

[20] Sobiesiak, L. A., and Damaren, C. J., "Lorentz-Augmented Spacecraft Formation Reconfiguration," *IEEE Transactions on Control Systems Technology*, Vol. 24, No. 2, 2016, pp. 514–524.
https://doi.org/10.1109/TCST.2015.2461593

[21] Sobiesiak, L. A., and Damaren, C. J., "Optimal Continuous/Impulsive Control for Lorentz-Augmented Spacecraft Formations," *Journal of Guidance, Control, and Dynamics*, Vol. 38, No. 1, 2015, pp. 151–157.
https://doi.org/10.2514/1.G000334

[22] Huang, X., Yan, Y., and Zhou, Y., "Neural Network-Based Adaptive Second Order Sliding Mode Control of Lorentz-Augmented Spacecraft Formation," *Neurocomputing*, Vol. 222, Jan. 2017, pp. 191–203.
https://doi.org/10.1016/j.neucom.2016.10.021

[23] Dang, Z., and Zhang, Y., "Relative Position and Attitude Estimation for Inner-Formation Gravity Measurement Satellite System," *Acta Astronautica*, Vol. 69, Nos. 7–8, 2011, pp. 514–525.
https://doi.org/10.1016/j.actaastro.2011.05.006

[24] De Angelis, A. G., Giulietti, F., de Ruiter, A. H. J., and Avanzini, G., "Spacecraft Attitude Control Using Magnetic and Mechanical Actuation," *Journal of Guidance, Control, and Dynamics*, Vol. 39, No. 3, 2016, pp. 564–573.
https://doi.org/10.2514/1.G000957

[25] Zhou, J., and Wen, C., *Adaptive Backstepping Control of Uncertain Systems*, Springer, Heidelberg, 2008, Chap. 2.
https://doi.org/10.1007/978-3-540-77807-3

[26] Huang, X., Yan, Y., and Zhou, Y., "Nonlinear Control of Underactuated Spacecraft Hovering," *Journal of Guidance, Control, and Dynamics*, Vol. 39, No. 3, 2016, pp. 685–694.
https://doi.org/10.2514/1.G001306

[27] Streetman, B., and Peck, M. A., "General Bang–Bang Control Method for Lorentz Augmented Orbits," *Journal of Spacecraft and Rockets*, Vol. 47, No. 3, 2010, pp. 484–492.
https://doi.org/10.2514/1.45704